

Stabilizing solitons of the cubic-quintic nonlinear Schrödinger equation by frequency-dependent linear gain-loss and delayed Raman response

Avner Peleg¹ and Debananda Chakraborty²

¹ Department of Mathematics, Azrieli College of Engineering, Jerusalem 9371207, Israel and

² Department of Mathematics, New Jersey City University, Jersey City, NJ 07305, USA

(Dated: March 22, 2023)

Abstract

We demonstrate transmission stabilization against radiation emission by frequency-dependent linear gain-loss and perturbation-induced frequency shifting for solitons of the cubic-quintic nonlinear Schrödinger (CQNLS) equation. We consider soliton propagation in a nonlinear optical waveguide with focusing cubic nonlinearity, defocusing quintic nonlinearity, and dissipative perturbations due to weak frequency-dependent linear gain-loss, cubic loss, and delayed Raman response. The frequency shifting is induced by delayed Raman response. Our perturbation analysis and numerical simulations with the perturbed CQNLS equation show that transmission stabilization with CQNLS solitons is indeed possible, and in this way provide the first demonstration of the stabilization method for solitons of a nonintegrable nonlinear wave model. Moreover, we find that transmission stabilization with energetic CQNLS solitons is realized with significantly smaller frequency shifts and pulse distortion compared with stabilization with energetic solitons of the cubic nonlinear Schrödinger equation. Therefore, our study also demonstrates that stabilization of energetic solitons by the method is significantly improved by the presence of defocusing quintic nonlinearity.

Keywords: Soliton, nonlinear Schrödinger equation, soliton stabilization, quintic nonlinearity, dissipative perturbations, perturbation method.

I. INTRODUCTION

The cubic-quintic nonlinear Schrödinger (CQNLS) equation is a simple nonintegrable generalization of the integrable cubic nonlinear Schrödinger (CNLS) equation [1–3]. It describes the behavior of a variety of physical systems, including the propagation of optical pulses in nonlinear semiconductor-doped optical waveguides [3–8], the propagation of optical beams in certain nonlinear bulk optical media [2, 9, 10] and thin films [11], the dynamics of Bose-Einstein condensates [12–15], and a range of interaction phenomena in plasmas [16–18]. It is also a simple model of pattern formation [1, 19], which describes, for example, the formation of fronts from pulses in the presence of deterministic or stochastic perturbations [19–22]. Since the CQNLS equation is a nonintegrable model, its investigation allows one to uncover physical effects that do not exist in the integrable CNLS model, or dynamic behavior that is qualitatively different from the one observed in the integrable case. Examples for the latter behavior include radiation-induced decay of solitons due to the existence of internal modes [23, 24], radiation emission in fast two-soliton collisions [25, 26], and emergence of spatiotemporal chaos [16, 27]. Due to all these reasons, the study of the CQNLS equation and its soliton solutions received great attention in the last few decades, and it is still a very active area of research. Examples of works on this subject include investigation of stability of soliton solutions in dimension 1 [1, 23, 24, 28–30] and in higher dimensions [1, 31], studies of soliton collisions and interaction [25, 26, 32, 33], investigation of soliton dynamics in confining potentials [14, 15, 34], and studies of highly nonlinear dynamic behavior that is described by the equation and by related equations [16, 18, 27].

In the current paper, we are interested in stabilizing the long-distance transmission of CQNLS solitons in the presence of weak linear and nonlinear dissipative perturbations in dimension 1. Since we are interested in transmission stabilization, we consider soliton propagation in the presence of focusing cubic nonlinearity and defocusing quintic nonlinearity. In this case, it is known that the unperturbed CQNLS equation in dimension 1 possesses stable soliton solutions, which exist for values of the amplitude parameter η satisfying $0 < \eta < \eta_m$, where the constant η_m depends on the quintic nonlinearity coefficient [1, 3, 5, 21, 23, 28]. Additionally, when η is near η_m , the soliton solutions attain a flat-top shape [21, 22]. Stability properties of CQNLS solitons in dimension 1 were studied in a number of works, see Refs. [1, 19, 23, 24, 28–30], and references therein. Importantly, orbital stability of soli-

tons of the unperturbed CQNLS equation with focusing cubic nonlinearity and defocusing quintic nonlinearity was proved in Ref. [28] for any η satisfying $0 < \eta < \eta_m$. Additionally, asymptotic stability of these solitons was proved in Ref. [29] for small-to-intermediate values of η . In Ref. [30], stability was established by considering the Hamiltonian-versus-energy diagram for the solitons. Furthermore, in Ref. [23] it was shown that there are no internal modes for CQNLS solitons in the case of focusing cubic nonlinearity and defocusing quintic nonlinearity, a result that leads to considerable simplification of the proof of their asymptotic stability [29]. Therefore, the studies in Refs. [23, 28–30] showed that solitons of the unperturbed CQNLS equation with focusing cubic nonlinearity and defocusing quintic nonlinearity in dimension 1 exhibit certain enhanced stability properties. From the physical point of view, the enhanced stability might be attributed to the fact that for these solitons, the effects of focusing cubic nonlinearity are balanced by both second-order dispersion and defocusing quintic nonlinearity [6, 35].

In Ref. [36], we developed a method for transmission stabilization of solitons of the CNLS equation that propagate in the presence of weak linear and nonlinear dissipative perturbations. Due to the presence of perturbations the CNLS soliton emits small-amplitude waves (radiation). These small-amplitude waves can grow and interact with the soliton, and this can lead to distortion of the soliton’s shape and to transmission destabilization [36–39]. The stabilization method that we developed in Ref. [36] was based on the interplay between perturbation-induced shifting of the soliton’s frequency and frequency-dependent linear gain-loss. In this method, the perturbation-induced shifting of the soliton’s frequency leads to the separation of the soliton’s Fourier spectrum from the radiation’s Fourier spectrum, and the frequency-dependent linear gain-loss leads to efficient suppression of radiation emission. We demonstrated the stabilization method for CNLS solitons with moderate power in two physically relevant nonlinear optical waveguide setups. In the first setup, the frequency shifting was caused by delayed Raman response, and in the second setup, the frequency shifting was caused by guiding filters with a varying central frequency [36]. Our numerical simulations with the two perturbed CNLS equations validated the method, and showed stable long-distance transmission of solitons with moderate power with very weak pulse distortion [36]. It should be pointed out that the method that we developed in Ref. [36] generalized a method that was theoretically and experimentally used in the 1990s to stabilize soliton transmission in nonlinear optical fibers in the presence of weak linear loss, linear

amplifier gain, and weak linear amplifier noise [40–42]. Therefore, our stabilization method is also very interesting from the experimental and the application points of view.

The study in Ref. [36] was limited to solitons of the integrable CNLS equation. Therefore, it is unclear if the stabilization method works for solitons of nonintegrable nonlinear wave models, such as the CQNLS equation. Additionally, it is unclear whether soliton stability is enhanced or reduced in the nonintegrable model compared with the integrable one. Furthermore, in Ref. [36] and in Refs. [40–42], only CNLS solitons with moderate power values were considered. Therefore, it is also unclear if the stabilization method works for solitons with high power values. The moderate power assumption is valid for the optical fiber transmission application. However, this assumption is definitely insufficient for nonlinear optical waveguide setups, where intermediate and strongly nonlinear amplitude dynamics is observed, see Refs. [39, 43] for examples of such waveguide setups.

In the current paper, we address the important questions listed in the preceding paragraph. More specifically, we investigate the propagation of a highly energetic CQNLS soliton in a nonlinear optical waveguide with focusing cubic nonlinearity, defocusing quintic nonlinearity, and three weak perturbations due to weak linear gain-loss, cubic loss, and delayed Raman response. The shifting of the soliton’s frequency is caused by the Raman perturbation. We assume a typical waveguide transmission system, in which the weak linear gain-loss counteracts the effects of weak cubic loss, such that the value of the soliton’s amplitude tends to an equilibrium value. We consider two different types of linear gain-loss: (1) frequency-independent linear gain; (2) frequency-dependent linear gain-loss. For each type of gain-loss, we use perturbative calculations to derive equations for the dynamics of the CQNLS soliton’s amplitude and frequency in the presence of the three perturbations. Furthermore, we perform numerical simulations with the perturbed CQNLS equation and characterize the distortion of the pulse shape and the Fourier spectrum. Additionally, we compare the simulations results with results of numerical simulations for propagation of a highly energetic CNLS soliton in similar waveguide setups in the absence of quintic nonlinearity.

In the case of waveguides with frequency-independent linear gain, we find that the transmission of an energetic CQNLS soliton and the dynamics of its amplitude and frequency parameters become unstable due to radiation emission. More specifically, our numerical simulations show that the soliton’s and radiation’s Fourier spectra become separated due to the perturbation-induced frequency shift experienced by the CQNLS soliton. However,

due to the presence of frequency-independent linear gain and the lack of an efficient mechanism for radiation suppression, the emitted radiation forms a highly modulated hump that continues to grow and leads to transmission destabilization. A comparison with results of numerical simulations with the perturbed CNLS equation show that transmission instability is stronger for the CNLS soliton.

Significant enhancement of transmission stability of the energetic CQNLS soliton is demonstrated in waveguides with frequency-dependent linear gain-loss. In this case, our numerical simulations with the perturbed CQNLS equation show stable long-distance propagation of the soliton with almost no pulse distortion, and stable dynamics of its amplitude and frequency parameters in excellent agreement with the perturbation theory predictions. Suppression of pulse distortion is enabled by the separation of the soliton's and radiation's Fourier spectra due to the soliton's frequency shift, and by the efficient suppression of radiation emission due to the frequency-dependent linear gain-loss. Therefore, our numerical simulations and perturbative calculations provide the first demonstration of the transmission stabilization method for solitons of a nonintegrable nonlinear wave model, far from the integrable limit. Further numerical simulations with the perturbed CNLS equation indicate that the transmission of an energetic CNLS soliton in waveguides with frequency-independent linear gain-loss is stable as well. However, the pulse distortion and the perturbation-induced frequency shift of the CNLS soliton are significantly larger than the pulse distortion and the frequency shift of the CQNLS soliton. Therefore, our study also demonstrates that stabilization of energetic solitons by the method is significantly improved by the presence of defocusing quintic nonlinearity.

We choose to investigate soliton propagation in the presence of linear gain-loss and cubic loss, since these perturbations are very common in many optical waveguides, and are often the dominant dissipative processes in these systems. In this sense, linear gain-loss and cubic loss are central examples for dissipative perturbations in optical systems. Furthermore, linear gain or loss and cubic loss are also present in many pattern forming systems, which are described by the complex Ginzburg-Landau equation [19, 20, 44, 45]. In optical waveguides, the cubic loss arises due to two-photon absorption or gain/loss saturation [46–48]. Pulse propagation in the presence of cubic loss has been studied in many previous works, see Refs. [19, 20, 22, 36, 39, 46, 49–54], and references therein. The subject gained even more attention in recent years due to the importance of two-photon absorption in silicon

nanowaveguides, which are expected to play a key role in many applications in optoelectronic devices [46–48, 55]. Delayed Raman response is another major nonlinear dissipative perturbation in optical waveguides. It is associated with the finite time of nonlinear response of the waveguide’s medium to the propagation of light [4, 56, 57]. Its main effects on the propagation of a single CNLS soliton in an optical waveguide are a continuous downshift of the soliton’s frequency, which is known as the Raman self-frequency shift [4, 56–58], and the emission of radiation by the soliton [4, 59]. The Raman-induced self-frequency shift can be viewed as a nonlinear process, in which energy is transferred from higher frequency components of the pulse to its lower frequency components [4, 56]. More generally, the Raman perturbation can lead to destabilization of the transmission of CNLS solitons in optical waveguides [4, 38, 60]. However, in Ref. [36], we showed that one can use the interplay between the Raman-induced frequency shift of a CNLS soliton and frequency-dependent linear gain-loss to stabilize the long-distance transmission of a CNLS soliton. In the current work, we show that this transmission stabilization method also works for solitons of the nonintegrable CQNLS equation with focusing cubic nonlinearity and defocusing quintic nonlinearity. Furthermore, we demonstrate that the introduction of defocusing quintic nonlinearity leads to remarkable enhancement of transmission stability of highly energetic solitons.

The rest of the paper is organized in the following manner. In Sec. II A, we present the unperturbed CQNLS equation and discuss the properties of its soliton solutions. In Sec. II B, we study transmission stability and instability of energetic CQNLS and CNLS solitons in waveguides with weak frequency-independent linear gain, cubic loss, and delayed Raman response. In Sec. II C, we investigate transmission stabilization of energetic CQNLS solitons in waveguides with weak frequency-dependent linear gain-loss, cubic loss, and delayed Raman response. We also carry out a comparison with stabilization of energetic CNLS solitons in a similar waveguide setup without quintic nonlinearity. In Sec. III, we summarize our results. In Appendix A, we derive the equations for dynamics of the CQNLS soliton’s amplitude and frequency parameters for the different waveguide setups considered in the paper. Appendix B is reserved for a description of the methods used to evaluate transmission stability from the numerical simulations results.

II. DYNAMICS OF CQNLS SOLITONS IN THE PRESENCE OF LINEAR GAIN-LOSS, CUBIC LOSS, AND DELAYED RAMAN RESPONSE

A. The unperturbed CQNLS equation with defocusing quintic nonlinearity

Propagation of pulses of light in a nonlinear optical waveguide with second-order dispersion, focusing cubic nonlinearity, and defocusing quintic nonlinearity is described by the CQNLS equation [1–3, 23, 26]:

$$i\partial_z\psi + \partial_t^2\psi + 2|\psi|^2\psi - \epsilon_q|\psi|^4\psi = 0. \quad (1)$$

In Eq. (1), ψ is proportional to the envelope of the electric field, z is distance, t is time, and $\epsilon_q > 0$ is the defocusing quintic nonlinearity coefficient [61]. Equation (1) is a nonintegrable nonlinear wave model [1, 23], and therefore its solutions can exhibit dynamical behavior that is different from the behavior of solutions of integrable models. The equation supports soliton solutions of the form [1, 3, 5, 21, 23]

$$\psi_s(t, z) = \Psi_s(x) \exp(i\chi), \quad (2)$$

where

$$\Psi_s(x) = \sqrt{2}\eta \left[(1 - \eta^2/\eta_m^2)^{1/2} \cosh(2x) + 1 \right]^{-1/2}, \quad (3)$$

$\chi = \alpha - \beta(t - y) + (\eta^2 - \beta^2)z$, $x = \eta(t - y + 2\beta z)$, and $\eta_m = (4\epsilon_q/3)^{-1/2}$. The parameters η , β , y , and α in these solutions are related to the soliton's amplitude, frequency, position, and phase, respectively. The soliton solutions (2) exist for amplitude parameter values satisfying $0 < \eta < \eta_m$. Additionally, for η values near η_m the solitons possess high power and attain a flat-top shape [21, 22].

Stability properties of solitons of unperturbed CQNLS equations were studied in a number of works, see Refs. [1, 19, 23, 24, 28–30], and references therein. In particular, the orbital stability of the solitons (2) of Eq. (1) was proved in Ref. [28] for any $0 < \eta < \eta_m$. Furthermore, asymptotic stability of these solitons was established in Ref. [29] for small-to-intermediate η values. In Ref. [30], stability was shown by considering the Hamiltonian-versus-energy diagram for the solitons. Additionally, in Ref. [23] it was shown that there are no internal modes for the solitons (2), and this leads to considerable simplification of the proof of their asymptotic stability [29]. Thus, the works in Refs. [23, 28–30] showed that

the solitons (2) of the CQNLs equation (1) exhibit certain enhanced stability properties. In the current paper we address another important question concerning the stability properties of the solitons (2). More specifically, we investigate whether propagation of these solitons in the presence of perturbations, which typically lead to radiative instability, can be stabilized by the interplay between frequency-dependent linear gain-loss and perturbation-induced shifting of the solitons' frequency. Furthermore, we compare transmission stabilization of the CQNLs solitons by this method with transmission stabilization for CNLS solitons in the presence of the same destabilizing perturbations.

The power \mathcal{M} , the momentum \mathcal{P} , and the Hamiltonian \mathcal{H} are conserved by the unperturbed CQNLs equation (1). These physical quantities are expressed in terms of ψ in the following manner [1]:

$$\mathcal{M} = \int_{-\infty}^{\infty} dt |\psi|^2, \quad (4)$$

$$\mathcal{P} = i \int_{-\infty}^{\infty} dt (\psi \partial_t \psi^* - \psi^* \partial_t \psi), \quad (5)$$

and

$$\mathcal{H} = \int_{-\infty}^{\infty} dt \left(|\partial_t \psi|^2/2 - |\psi|^2/2 + \epsilon_q |\psi|^4/6 \right). \quad (6)$$

In general, \mathcal{M} , \mathcal{P} , and \mathcal{H} , are not conserved in the presence of *dissipative perturbations* to Eq. (1). As a result, in this case, the values of the soliton's parameters η and β might change with distance z . One can then obtain the equations for $d\eta/dz$ and $d\beta/dz$ by employing energy and momentum balance calculations, which are based on the expressions for \mathcal{M} and \mathcal{P} in Eqs. (4) and (5). In the next subsections, we study the dynamics of the CQNLs soliton and its parameters η and β in the presence of dissipative perturbations due to linear gain or loss, cubic loss, and delayed Raman response.

B. Soliton dynamics in the presence of frequency-independent linear gain, cubic loss, and delayed Raman response

We consider soliton propagation in a nonlinear optical waveguide with focusing cubic nonlinearity, defocusing quintic nonlinearity, weak frequency-independent linear gain, cubic loss, and delayed Raman response. Quintic nonlinearity and delayed Raman response are

both first-order corrections to cubic nonlinearity, and therefore, including both effects in the same propagation equation is consistent in terms of the mathematical modeling. The propagation is described by the following perturbed CQNLS equation [62]:

$$i\partial_z\psi + \partial_t^2\psi + 2|\psi|^2\psi - \epsilon_q|\psi|^4\psi = ig_0\psi/2 - i\epsilon_3|\psi|^2\psi + \epsilon_R\psi\partial_t|\psi|^2, \quad (7)$$

where the third term on the right hand side is due to delayed Raman response. The linear gain, cubic loss, and Raman coefficients, g_0 , ϵ_3 , and ϵ_R , satisfy $g_0 > 0$, $0 < \epsilon_3 \ll 1$, and $0 < \epsilon_R \ll 1$ [63, 64].

The equations for the dynamics of the amplitude and frequency parameters of the CQNLS soliton are obtained in Appendix A by employing energy balance and momentum balance calculations. These calculations yield the following equations:

$$\frac{d\eta}{dz} = \frac{(\eta_m^2 - \eta^2)}{\eta_m} \left\{ g_0 \operatorname{arctanh} \left(\frac{\eta}{\eta_m} \right) - 4\epsilon_3 \eta_m^2 \left[\operatorname{arctanh} \left(\frac{\eta}{\eta_m} \right) - \frac{\eta}{\eta_m} \right] \right\}, \quad (8)$$

and

$$\frac{d\beta}{dz} = \frac{-4\epsilon_R \eta_m^4}{3 \operatorname{arctanh}(\eta/\eta_m)} \left[\frac{3\eta}{\eta_m} - \frac{2\eta^3}{\eta_m^3} - 3 \left(1 - \frac{\eta^2}{\eta_m^2} \right) \operatorname{arctanh} \left(\frac{\eta}{\eta_m} \right) \right]. \quad (9)$$

Note that the amplitude shift in Eq. (8) is induced only by the effects of linear gain and cubic loss. Additionally, the frequency shift in Eq. (9) is induced solely by the Raman effect. Thus, Eq. (9) describes the soliton's Raman self-frequency shift in optical waveguides with focusing cubic nonlinearity and defocusing quintic nonlinearity.

In optical waveguide transmission systems it is usually desired to realize stable steady-state transmission with constant pulse amplitudes [4, 65]. We therefore require that $\eta = \eta_0$ with $0 < \eta_0 < \eta_m$ is a stable equilibrium point of Eq. (8), and obtain the following expression for g_0 :

$$g_0 = 4\epsilon_3 \eta_m^2 \left[1 - \frac{\eta_0/\eta_m}{\operatorname{arctanh}(\eta_0/\eta_m)} \right]. \quad (10)$$

Substitution of Eq. (10) into Eq. (8) yields

$$\frac{d\eta}{dz} = 4\epsilon_3 \eta_m^3 \left(1 - \frac{\eta^2}{\eta_m^2} \right) \operatorname{arctanh} \left(\frac{\eta}{\eta_m} \right) \left[\frac{\eta/\eta_m}{\operatorname{arctanh}(\eta/\eta_m)} - \frac{\eta_0/\eta_m}{\operatorname{arctanh}(\eta_0/\eta_m)} \right]. \quad (11)$$

One can show that $\eta = \eta_0$ is the only equilibrium point of Eq. (11) with a nonnegative amplitude value and that it is a stable equilibrium point. In the current work, we are particularly interested in transmission stabilization of energetic CQNLS solitons, which occurs

for η_0 values close to η_m . This means that we are studying transmission stabilization near the flat-top soliton limit of Eq. (1), which is also the front formation limit [21, 22].

It is useful to consider the form of Eqs. (11) and (9) in the following two cases. (1) The limit $\epsilon_q \rightarrow 0^+$ ($\eta_m \rightarrow \infty$) that corresponds to the CNLS limit. (2) The case where η is close to η_0 , and η_0 is close to η_m , i.e., for highly energetic CQNLS solitons near the flat-top soliton limit. In the limit $\epsilon_q \rightarrow 0^+$, we retrieve the equations for the amplitude shift and the Raman-induced self-frequency shift of the CNLS soliton (see Refs. [36, 56–58]):

$$\frac{d\eta}{dz} \simeq \frac{4}{3}\epsilon_3 (\eta_0^2 - \eta^2) \eta, \quad (12)$$

and

$$\frac{d\beta}{dz} \simeq -\frac{8}{15}\epsilon_R \eta^4. \quad (13)$$

In case (2), we denote $\eta = \eta_0 + \delta\eta$, where $|\delta\eta| \ll 1$, $\delta\eta < \eta_m - \eta_0$, and $\eta_0 \lesssim \eta_m$. We then expand the right hand sides of Eqs. (11) and (9) in Taylor series about η_0 , keeping only the leading term in each expansion. This approximation amounts to a linearization of Eq. (11) about the equilibrium point $\eta = \eta_0$, and to a calculation of the constant rate of change of β for $\eta = \eta_0$. We obtain:

$$\frac{d\eta}{dz} \simeq 4\epsilon_3 \left[(\eta_m^2 - \eta_0^2) - \frac{\eta_0 \eta_m}{\operatorname{arctanh}(\eta_0/\eta_m)} \right] \delta\eta, \quad (14)$$

and

$$\frac{d\beta}{dz} \simeq \frac{-4\epsilon_R \eta_m^4}{3\operatorname{arctanh}(\eta_0/\eta_m)} \left[\frac{3\eta_0}{\eta_m} - \frac{2\eta_0^3}{\eta_m^3} - 3 \left(1 - \frac{\eta_0^2}{\eta_m^2} \right) \operatorname{arctanh} \left(\frac{\eta_0}{\eta_m} \right) \right]. \quad (15)$$

Note that for η_0 values near η_m , the value of the expression inside the square brackets on the right hand side of Eq. (15) is close to 1, while the value of the denominator is much larger than 1. Therefore, according to the perturbation theory, in case (2), the rate of change of the CQNLS soliton's frequency due to the Raman effect tends to a *small* negative constant value at large distances. This behavior is strikingly different from the behavior expected for the CNLS soliton. Indeed, it follows from Eq. (13) that the rate of change of the CNLS soliton's frequency is not necessarily small for large η and η_0 values.

Numerical simulations. According to Eq. (11), the dynamics of the CQNLS soliton's amplitude is expected to be stable. However, this prediction is based on an energy-balance calculation, which neglects radiation emission effects. The latter effects can become important at intermediate and large distances, and they can lead to distortion of the soliton's

shape and to the breakdown of the energy-balance approximation used in the derivation of Eq. (11). This is particularly true for the optical waveguide setup considered here, since the presence of linear gain leads to unstable growth of small amplitude waves that are associated with radiation. For these reasons, it is important to check the validity of the predictions obtained with Eq. (9) and Eq. (11), and the stability of the CQNLS soliton in the presence of perturbations by numerical simulations with Eq. (7).

The setup of the numerical simulations with the perturbed CQNLS equation (7) is somewhat similar to the setup used in Ref. [36] for simulations with the perturbed CNLS equation. More specifically, we solve Eq. (7) numerically on a time domain $[t_{\min}, t_{\max}] = [-400, 400]$ using the split-step method with periodic boundary conditions [1, 4]. The initial input is in the form of the CQNLS soliton of Eq. (2) with amplitude parameter $\eta(0)$, frequency $\beta(0) = 0$, position $y(0) = 0$, and phase $\alpha(0) = 0$. Since we are interested in transmission stabilization near the flat-top soliton limit, we choose an η_0 value that is close to η_m . Therefore, the soliton's shape at equilibrium is not far from a flat-top shape. Additionally, the soliton's power at equilibrium is significantly larger than the equilibrium value of the soliton's power that was used in Ref. [36] for CNLS solitons. As a typical example, we consider here the results of the simulations with $\epsilon_q = 0.5$, $\epsilon_3 = 0.01$, $\epsilon_R = 0.04$, $\eta_0 = 1.2$, and $\eta(0) = 0.9$. We emphasize, however, that similar results are obtained with other values of the physical parameters. Note that the value $\eta_0 = 1.2$ is indeed close to the η_m value, $\eta_m = 1.2247\dots$. Additionally, the CQNLS soliton's power at equilibrium is $5.6172\dots$, which is significantly larger than the value 2 that was used in Ref. [36] for CNLS solitons. The application of periodic boundary conditions means that the simulations describe propagation in a closed optical waveguide loop. This setup is very relevant for applications, since most long-distance optical waveguide transmission experiments are carried out in closed loops, see, e.g., Refs. [41, 42, 66–68].

Transmission quality and pulse-shape distortion are measured from the simulations results by the transmission quality integral $I(z)$, which is defined in Eq. (B4) in Appendix B. $I(z)$ measures the deviation of the numerically obtained pulse shape $|\psi^{(num)}(t, z)|$ from the perturbation theory prediction $|\psi^{(th)}(t, z)|$ that is given by Eq. (B1). Therefore, $I(z)$ measures both distortion in the pulse shape due to radiation emission and deviations in the numerically obtained values of the soliton's parameters from the values predicted by Eqs. (9) and Eq. (11). Further insight into transmission quality and pulse-shape distortion is

obtained by measuring the distance z_q at which the value of $I(z)$ first exceeds 0.075. We refer to z_q as the transmission quality distance. Additionally, we characterize soliton stability and pulse-shape distortion at larger distances, by running the simulations up to a final distance z_f at which the value of $I(z)$ first exceeds 0.655 [69]. For the physical parameter values specified in the preceding paragraph, we find $z_q = 140$ and $z_f = 300$.

The pulse shape $|\psi(t, z)|$ obtained in the numerical simulation at $z = z_q$ and at $z = z_f$ is shown in Fig. 1. A comparison with the perturbation theory prediction of Eqs. (B1) and (11) is also shown. As seen in Fig. 1(a), the pulse shape obtained in the simulation at $z = z_q$ is close to the perturbation theory prediction. However, the comparison in Figs. 1(b) and 1(c) for small $|\psi(t, z_q)|$ values shows that a noticeable radiative tail exists already at this distance. This radiative tail, which is induced by the three perturbation terms in Eq. (7), is highly oscillatory and is spread over the entire computational domain. It attains the form of a highly modulated hump. As the soliton continues to propagate, the radiative tail continues to grow [see Figs. 1(d)-1(f)]. Furthermore, as seen in Fig. 2, the growth of the radiative tail leads to the increase of the value of the transmission quality integral $I(z)$ with increasing z .

Further insight into pulse-shape distortion and soliton instability is gained by considering the shape of the Fourier spectrum $|\hat{\psi}(\omega, z)|$. The numerically obtained spectrum $|\hat{\psi}(\omega, z)|$ at $z = z_q$ and at $z = z_f$ is shown in Fig. 3 along with the perturbation theory prediction of Eqs. (B3), (9), and (11). It is seen that the soliton's Fourier spectrum is centered around the z dependent soliton's frequency $\beta(z)$, and is shifted relative to the radiation's spectrum, which is centered near $\omega = 0$ and is growing with increasing z . The separation of the soliton and radiation spectra, which is clear already at $z = z_q$ [see Figs. 3(a) - 3(c)], is a result of the Raman-induced self-frequency shift experienced by the soliton. It grows with increasing z due to the increase in $|\beta(z)|$ [compare Figs. 3(a) and 3(d)]. Due to the separation between the two spectra, the soliton part of the numerically obtained graph of $|\hat{\psi}(\omega, z)|$ is very close to the perturbation theory prediction [see Figs. 3(c) and 3(e)]. However, the growth of the radiation spectrum with increasing z leads to the strong oscillatory distortion in the pulse shape and to the soliton destabilization seen in Figs. 1 and 2.

The destabilization of the CQNLS soliton in the current waveguide setup is also evident in the dynamics of the soliton's amplitude and frequency. Figure 4 shows the z dependence of the soliton's amplitude and frequency obtained in the simulation together with the pertur-

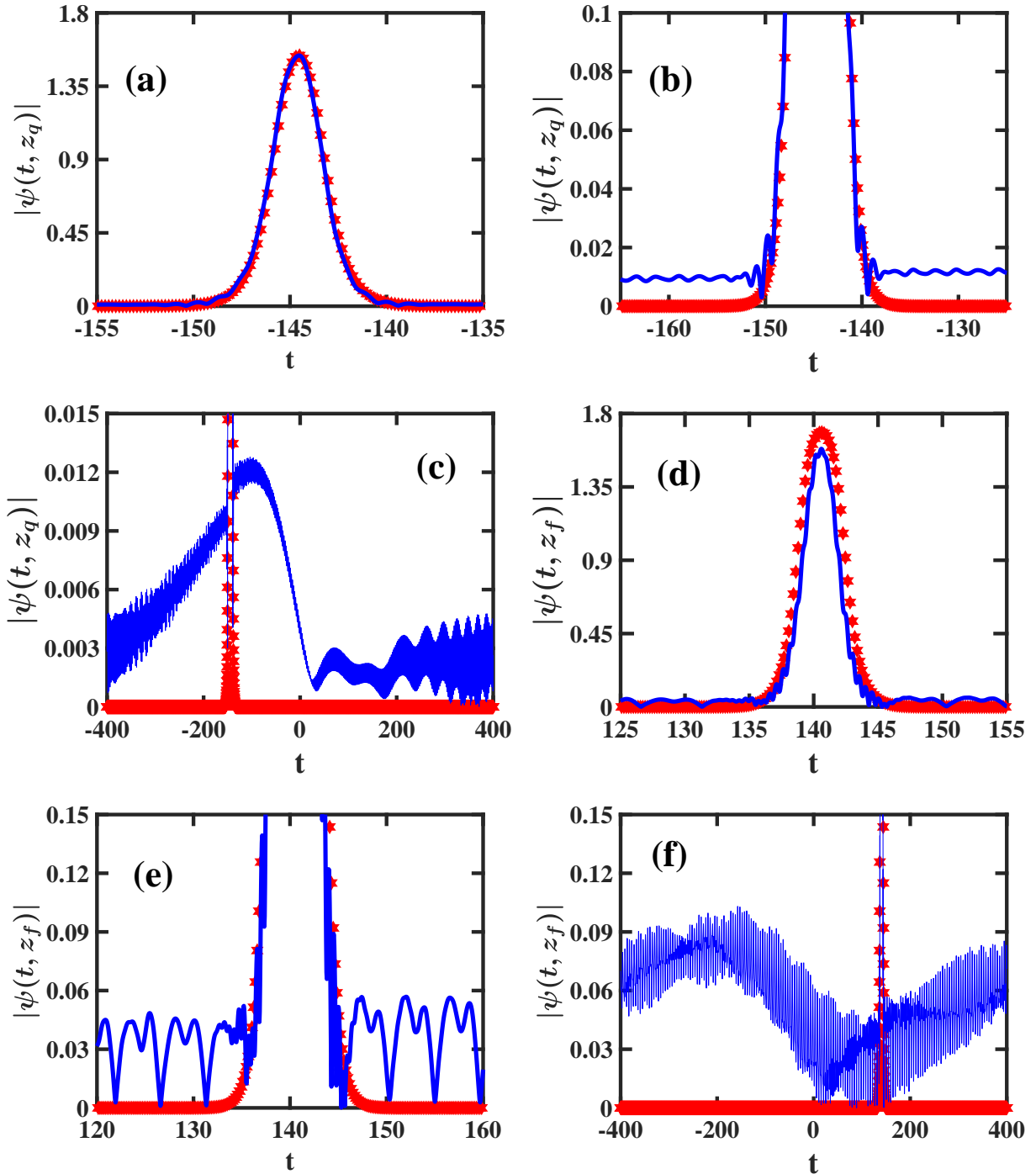


FIG. 1: The pulse shape $|\psi(t, z)|$ at $z_q = 140$ [(a), (b), (c)] and at $z_f = 300$ [(d), (e), (f)] for propagation of a CQNLS soliton in a waveguide loop with weak frequency-independent linear gain, cubic loss, and delayed Raman response. The physical parameter values are $\epsilon_q = 0.5$, $\epsilon_3 = 0.01$, $\epsilon_R = 0.04$, $\eta_0 = 1.2$, and $\eta(0) = 0.9$. The solid blue curve represents the result obtained by the numerical simulation with Eq. (7). The red stars correspond to the perturbation theory prediction, obtained with Eqs. (B1) and (11).

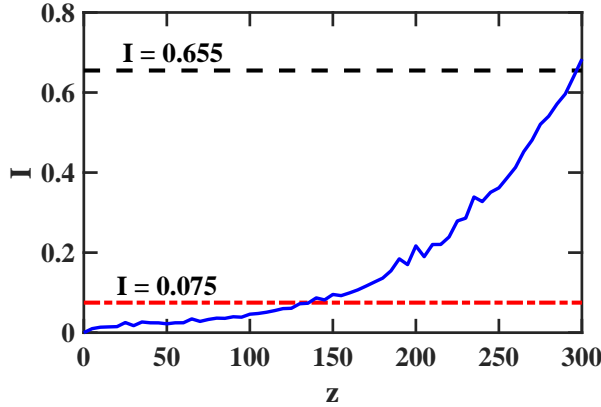


FIG. 2: The z dependence of the transmission quality integral $I(z)$ obtained by the numerical simulation with Eq. (7) for the same waveguide setup as in Fig. 1. The solid blue curve stands for the simulation's result. The dashed black and dashed-dotted red horizontal lines correspond to $I = 0.655$ and $I = 0.075$, respectively.

bation theory predictions of Eqs. (11) and (9). In both graphs we observe good agreement between the simulation's results and the predictions of Eqs. (11) and (9) for $0 \leq z \leq 200$. In particular, we see that in this interval, the numerically obtained amplitude value tends to the equilibrium value $\eta_0 = 1.2$. However, for $200 < z \leq 300$, the numerical curve of $\eta(z)$ deviates from the prediction of Eq. (11) and the numerical curve of $\beta(z)$ deviates significantly from the prediction of Eq. (9). These increasing deviations coincide with the increase in pulse-shape distortion and in the value of $I(z)$ observed in Figs. 1 and 2. Thus, based on the results presented in Figs. 1-4 and on similar results obtained with other values of the physical parameters we conclude that transmission of the CQNLS soliton in waveguide loops with weak frequency-independent linear gain, cubic loss, and delayed Raman response is unstable.

Comparison with transmission stability of the CNLS soliton. It is useful to compare the results of the simulation for transmission stability of the CQNLS soliton with the results of numerical simulations for transmission stability of the CNLS soliton in the same optical waveguide setup. For this purpose, we carry out numerical simulations with the following perturbed CNLS model [36]:

$$i\partial_z\psi + \partial_t^2\psi + 2|\psi|^2\psi = ig_0\psi/2 - i\epsilon_3|\psi|^2\psi + \epsilon_R\psi\partial_t|\psi|^2, \quad (16)$$

which is similar to Eq. (7), except for the absence of the quintic nonlinearity term. We

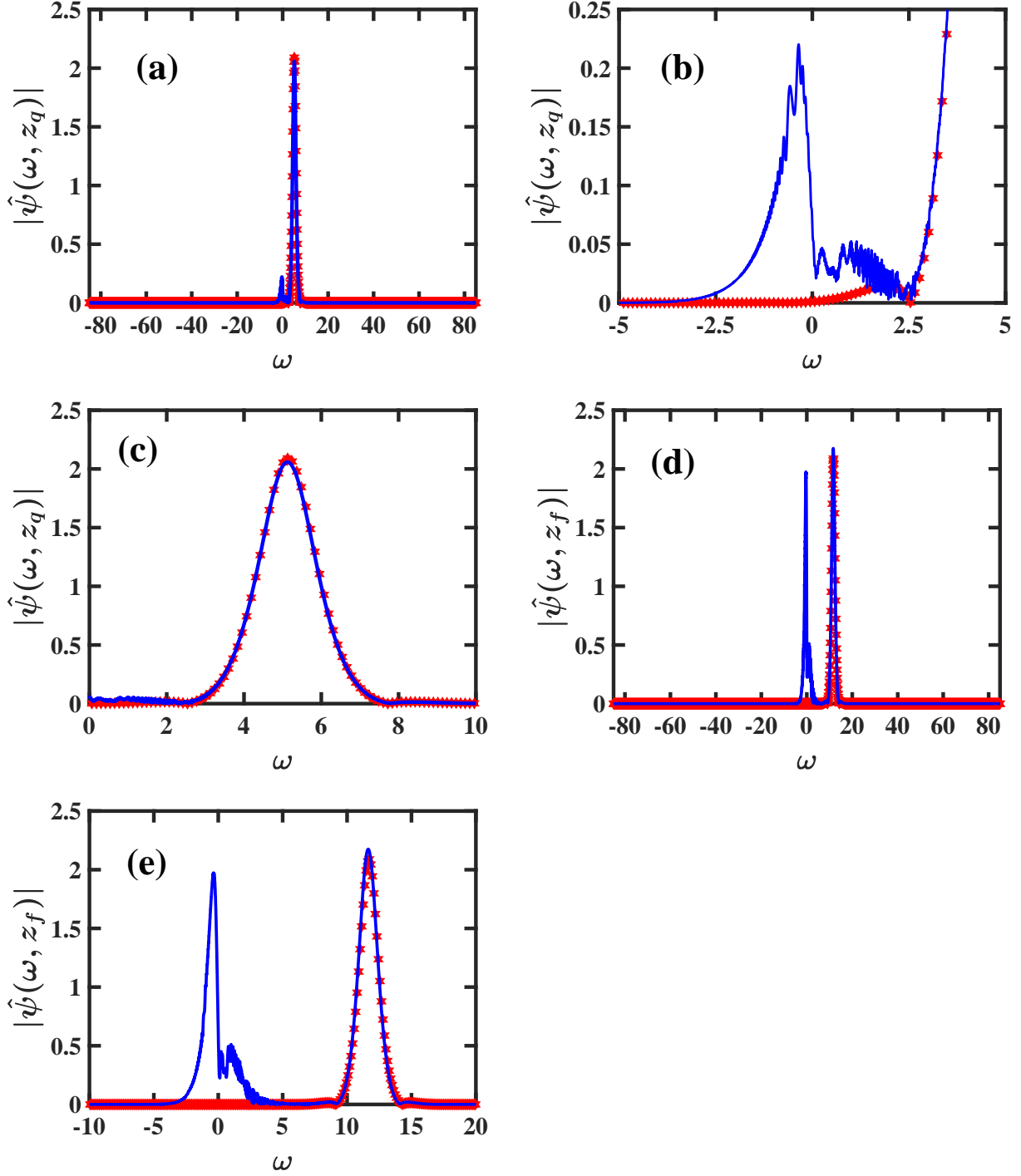


FIG. 3: The shape of the Fourier spectrum $|\hat{\psi}(\omega, z)|$ at $z_q = 140$ [(a), (b), (c)] and at $z_f = 300$ [(d), (e)] for propagation of a CQNLS soliton in a waveguide loop with weak frequency-independent linear gain, cubic loss, and delayed Raman response. The physical parameter values are the same as in Fig. 1. The solid blue curve represents the result obtained by numerical solution of Eq. (7), and the red stars correspond to the perturbation theory prediction of Eqs. (B3), (9), and (11).

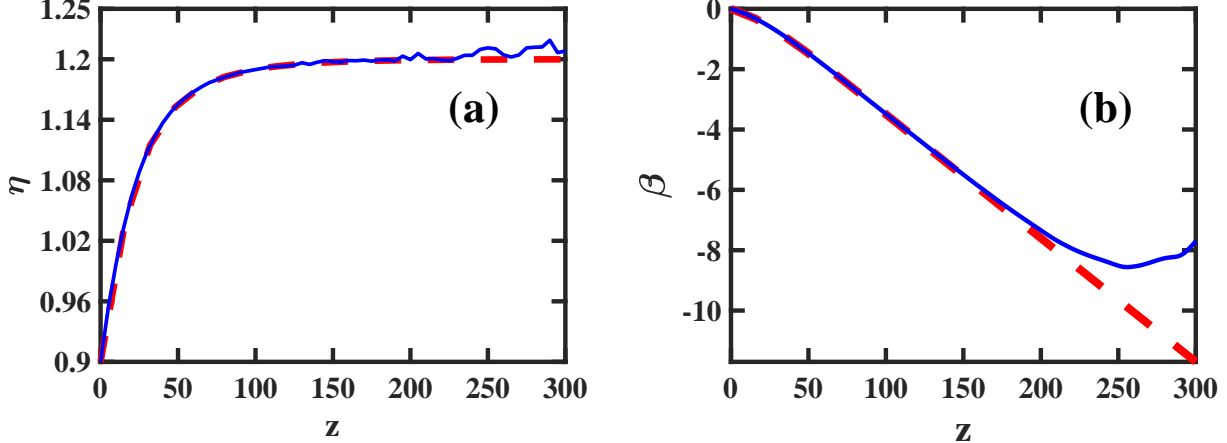


FIG. 4: The z dependence of the CQNLS soliton's amplitude $\eta(z)$ (a) and frequency $\beta(z)$ (b) for the same waveguide setup as in Figs. 1-3. The solid blue curves represent the results obtained by numerical solution of Eq. (7). The dashed red curves correspond to the perturbation theory predictions of Eq. (11) in (a) and of Eqs. (9) and (11) in (b).

consider an initial condition in the form of the fundamental soliton of the CNLS equation

$$\psi_s^{(c)}(t, z) = \eta^{(c)} \exp(i\chi) / \cosh(x), \quad (17)$$

where $x = \eta^{(c)}(t - y^{(c)} + 2\beta^{(c)}z)$, $\chi = \alpha^{(c)} - \beta^{(c)}(t - y^{(c)}) + (\eta^{(c)2} - \beta^{(c)2})z$, and $\eta^{(c)}$, $\beta^{(c)}$, $y^{(c)}$, and $\alpha^{(c)}$ are the CNLS soliton's amplitude, frequency, position, and phase.

By the adiabatic perturbation theory for the CNLS soliton, the dynamics of the soliton's amplitude and frequency is described by [36]:

$$\frac{d\eta^{(c)}}{dz} = \frac{4}{3}\epsilon_3 \left(\eta_0^{(c)2} - \eta^{(c)2} \right) \eta^{(c)}, \quad (18)$$

and

$$\frac{d\beta^{(c)}}{dz} = -\frac{8}{15}\epsilon_R \eta^{(c)4}, \quad (19)$$

where $\eta_0^{(c)}$ is the amplitude value at stable equilibrium, and $g_0 = 4\epsilon_3\eta_0^{(c)2}/3$ is used. Therefore, $\eta^{(c)}(z)$ and $\beta^{(c)}(z)$ are given by:

$$\eta^{(c)}(z) = \eta_0^{(c)} \left[1 + \left(\frac{\eta_0^{(c)2}}{\eta^{(c)2}(0)} - 1 \right) \exp \left(-8\epsilon_3\eta_0^{(c)2}z/3 \right) \right]^{-\frac{1}{2}}, \quad (20)$$

and

$$\beta^{(c)}(z) = \beta^{(c)}(0) - \frac{\epsilon_R \eta_0^{(c)2}}{5\epsilon_3} \left\{ \ln \left[\frac{\eta_0^{(c)2} - \eta^{(c)2}(0) + \eta^{(c)2}(0) \exp \left(8\epsilon_3 \eta_0^{(c)2} z / 3 \right)}{\eta_0^{(c)2}} \right] \right. \\ \left. + \frac{\eta^{(c)2}(0)}{\eta_0^{(c)2}} - \frac{\eta^{(c)2}(0)}{\eta^{(c)2}(0) + [\eta_0^{(c)2} - \eta^{(c)2}(0)] \exp \left(-8\epsilon_3 \eta_0^{(c)2} z / 3 \right)} \right\}. \quad (21)$$

Equation (16) is solved numerically on a time domain $[t_{\min}, t_{\max}] = [-400, 400]$ with periodic boundary conditions. The initial condition is in the form of the CNLS soliton in Eq. (17) with parameter values $\eta^{(c)}(0)$, $\beta^{(c)}(0) = 0$, $y^{(c)}(0) = 0$, and $\alpha^{(c)}(0) = 0$. To make a meaningful comparison with the results presented in Figs. 1-4, we use the parameter values $\epsilon_3 = 0.01$ and $\epsilon_R = 0.04$. Additionally, we require that the initial power and the equilibrium power of the CNLS soliton would be equal to the initial power and the equilibrium power of the CQNLs soliton, respectively. That is, we determine the values of $\eta^{(c)}(0)$ and $\eta_0^{(c)}$ that should be used in the CNLS simulation by requiring: $2\eta^{(c)}(0) = 2\eta_m \operatorname{arctanh} [\eta(0)/\eta_m]$ and $2\eta_0^{(c)} = 2\eta_m \operatorname{arctanh} (\eta_0/\eta_m)$, where $\eta(0)$ and η_0 are the values of the initial amplitude and the equilibrium amplitude used in the CQNLs simulation. For the values $\eta_m = 1.2247\dots$, $\eta_0 = 1.2$, and $\eta(0) = 0.9$ used in the CQNLs simulation, we obtain: $\eta_0^{(c)} = 2.8086\dots$ and $\eta^{(c)}(0) = 1.1503\dots$

The values of the transmission quality distance and the final propagation distance obtained in the simulation with Eq. (16) are $z_q = 20$ and $z_f = 76$. These values are significantly smaller compared with the values $z_q = 140$ and $z_f = 300$, obtained for the CQNLs soliton. As we will see in the next paragraphs, the reduction in the values of z_q and z_f for the CNLS soliton is due to the fact that the radiation-induced pulse distortion effects in this case are significantly stronger than the pulse distortion effects observed for the CQNLs soliton in Figs. 1-4.

We consider first the dynamics of the radiation-induced pulse distortion for the CNLS soliton. Figure 5 shows the pulse shape $|\psi(t, z)|$ obtained in the simulation with Eq. (16) at $z = z_q$ and $z = z_f$ together with the prediction of the perturbation theory, which is given by Eqs. (B5) and (20). As seen in Figs. 5(a)-5(c), the numerical result for the pulse shape at $z = z_q$ is close to the perturbation theory prediction, but an appreciable radiative tail is present already at this distance. We note that the main part of the radiative tail forms a double hump, which is more pronounced than the radiative hump that is formed for the

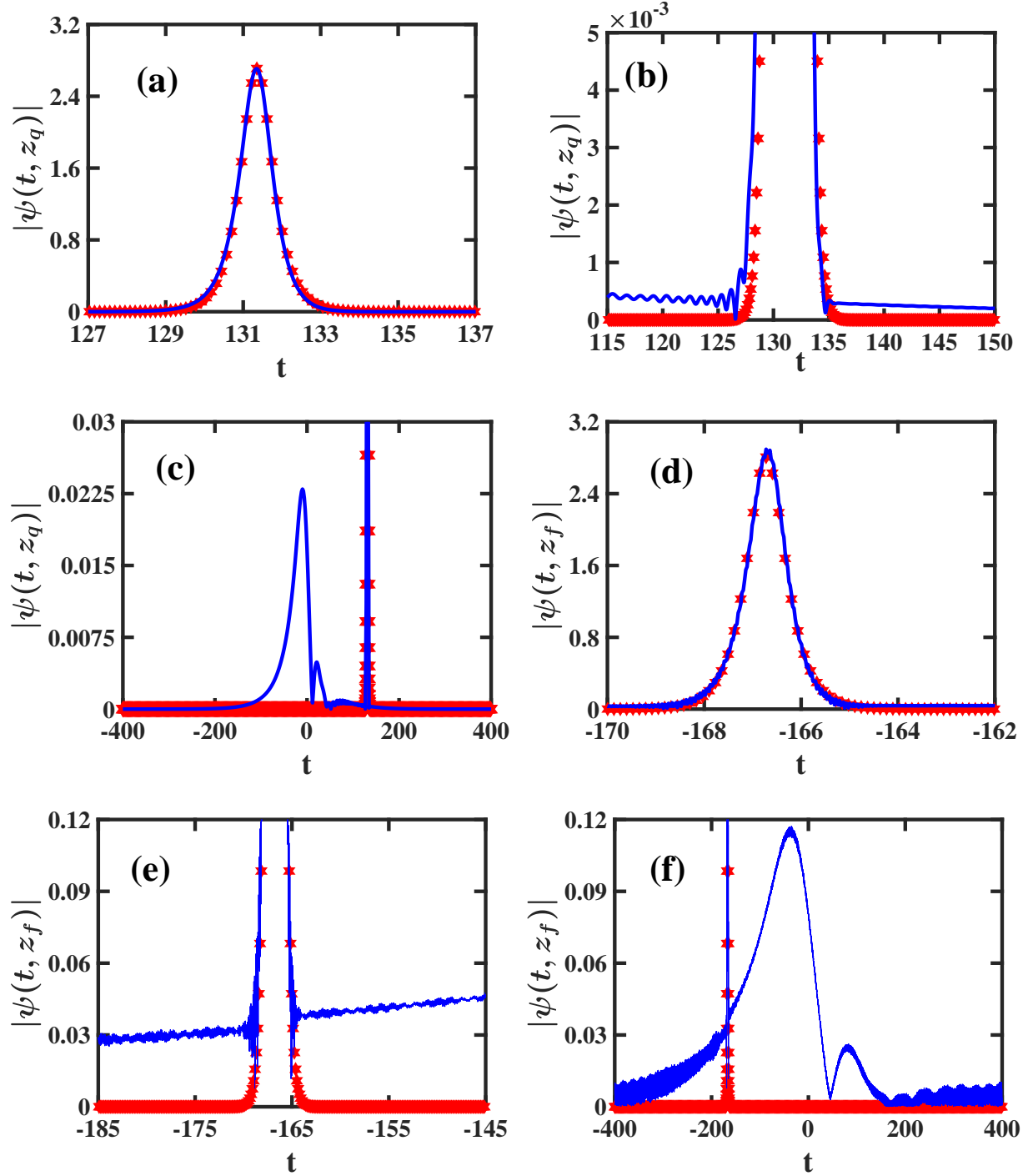


FIG. 5: The pulse shape $|\psi(t, z)|$ at $z_q = 20$ [(a), (b), (c)] and at $z_f = 76$ [(d), (e), (f)] for propagation of a CNLS soliton in a waveguide loop with weak frequency-independent linear gain, cubic loss, and delayed Raman response. The parameter values are $\epsilon_3 = 0.01$, $\epsilon_R = 0.04$, $\eta_0^{(c)} = 2.8086\dots$ and $\eta^{(c)}(0) = 1.1503\dots$. The solid blue curve represents the result obtained by numerical solution of Eq. (16). The red stars correspond to the perturbation theory prediction, obtained with Eqs. (B5) and (20).

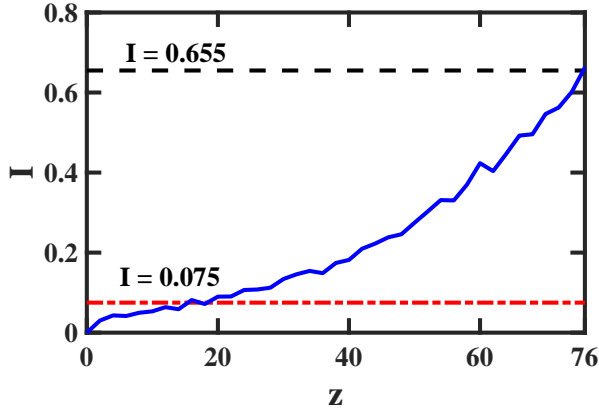


FIG. 6: The z dependence of the transmission quality integral $I(z)$ obtained by the numerical simulation with Eq. (16) for the waveguide setup considered in Fig. 5. The solid blue curve represents the simulation's result. The dashed black and dashed-dotted red horizontal lines correspond to $I = 0.655$ and $I = 0.075$, respectively.

CQNLS soliton. We also note that the part of the radiative tail near the CNLS soliton is weaker (smaller) than the corresponding part of the radiative tail for the CQNLS soliton. Moreover, as seen in 5(d)-5(f), the radiative tail of the CNLS soliton grows significantly with increasing distance [70]. As a result, the transmission quality integral increases significantly and exceeds the value 0.655 at $z_f = 76$ (see Fig. 6).

The shape of the Fourier spectrum $|\hat{\psi}(\omega, z)|$ provides valuable insight into pulse-shape distortion and soliton instability. Figure 7 shows the simulation's result for the Fourier spectrum at $z = z_q$ and at $z = z_f$ together with the perturbation theory prediction of Eqs. (B6), (20), and (21). Similar to the CQNLS case, the soliton's and radiation's spectra are separated already at $z = z_q$ due to the Raman-induced self-frequency shift experienced by the CNLS soliton. Accordingly, the soliton's spectrum is centered around $\beta^{(c)}(z)$, while the main part of the radiation's spectrum is centered near $\omega = 0$ [see Figs. 7(a)-7(c)]. As the soliton continues to propagate along the waveguide, the radiation's spectrum grows significantly, and a new radiative peak, which was not observed in the CQNLS case, appears near $\omega = -100$ [see Figs. 7(d)-7(f)]. Additionally, the separation between the soliton's and radiation's spectra increases significantly, and is much larger at $z = z_f$ than the spectral separation that was observed for the CQNLS soliton. Due to this spectral separation, the soliton part of the numerical result for $|\hat{\psi}(\omega, z)|$ is not distorted, i.e., its shape is close to the one predicted by the perturbation theory [see Figs. 7(c) and 7(f)]. However, the

growth of the radiative spectrum leads to the strong pulse distortion and to the transmission destabilization that are observed in Figs. 5 and 6. We also note that the numerical curve of $|\hat{\psi}(\omega, z_f)|$ is shifted considerably to the right compared with the theoretical curve. This shift can be explained by noting that since $\eta_0^{(c)} = 2.8086\dots$, the CNLS soliton attains large amplitude values at large distances. As a result, the Raman perturbation term in Eq. (16) is not weak at these distances, and its effects are larger than the effects predicted by the perturbation theory.

The effects of pulse distortion and transmission destabilization for the CNLS soliton can also be detected by following the dynamics of its amplitude and frequency. Figures 8(a) and 8(b) show the z dependence of the soliton's amplitude and frequency obtained in the simulation together with the perturbation theory predictions of Eqs. (20) and (21). We observe that for $0 \leq z \leq 50$, the simulation's results for $\eta^{(c)}$ and $\beta^{(c)}$ are in good agreement with the perturbation theory predictions. However, for $50 < z \leq 76$, the numerical results deviate significantly from the perturbation theory predictions. In particular, the absolute differences between the theoretical and numerical results at $z = z_f$ are $|\eta^{(c)(th)}(z_f) - \eta^{(c)(num)}(z_f)| = 0.7670\dots$ and $|\beta^{(c)(th)}(z_f) - \beta^{(c)(num)}(z_f)| = 14.79\dots$. These values are significantly larger than the corresponding differences that were obtained for the CQNLS soliton: $|\eta^{(th)}(z_f) - \eta^{(num)}(z_f)| = 0.0083\dots$ and $|\beta^{(th)}(z_f) - \beta^{(num)}(z_f)| = 3.99\dots$. The increasing deviations between the numerical and theoretical results for $\eta^{(c)}$ and $\beta^{(c)}$ occur together with the increase in pulse-shape distortion and in the value of $I(z)$, which are seen in Figs. 5 and 6. Therefore, the results for amplitude and frequency dynamics together with the results shown in Figs. 5-7 and similar results obtained with other physical parameter values show that transmission of the CNLS soliton in waveguide loops with weak frequency-independent linear gain, cubic loss, and delayed Raman response is unstable. We also note that both the numerical and the theoretical values of the CNLS soliton's frequency $\beta^{(c)}(z)$ are much larger than the frequency values $\beta(z)$ observed for the CQNLS soliton. This finding is in agreement with the prediction of Eq. (15) for the decrease in the rate of change of the Raman self-frequency shift of the CQNLS soliton for η and η_0 values near η_m .

Summary. It is worthwhile to summarize the features of pulse dynamics, which show that pulse distortion and transmission destabilization are stronger for the CNLS soliton than for the CQNLS soliton.

1. *Transmission quality distances.* The distances z_q and z_f , which characterize transmis-

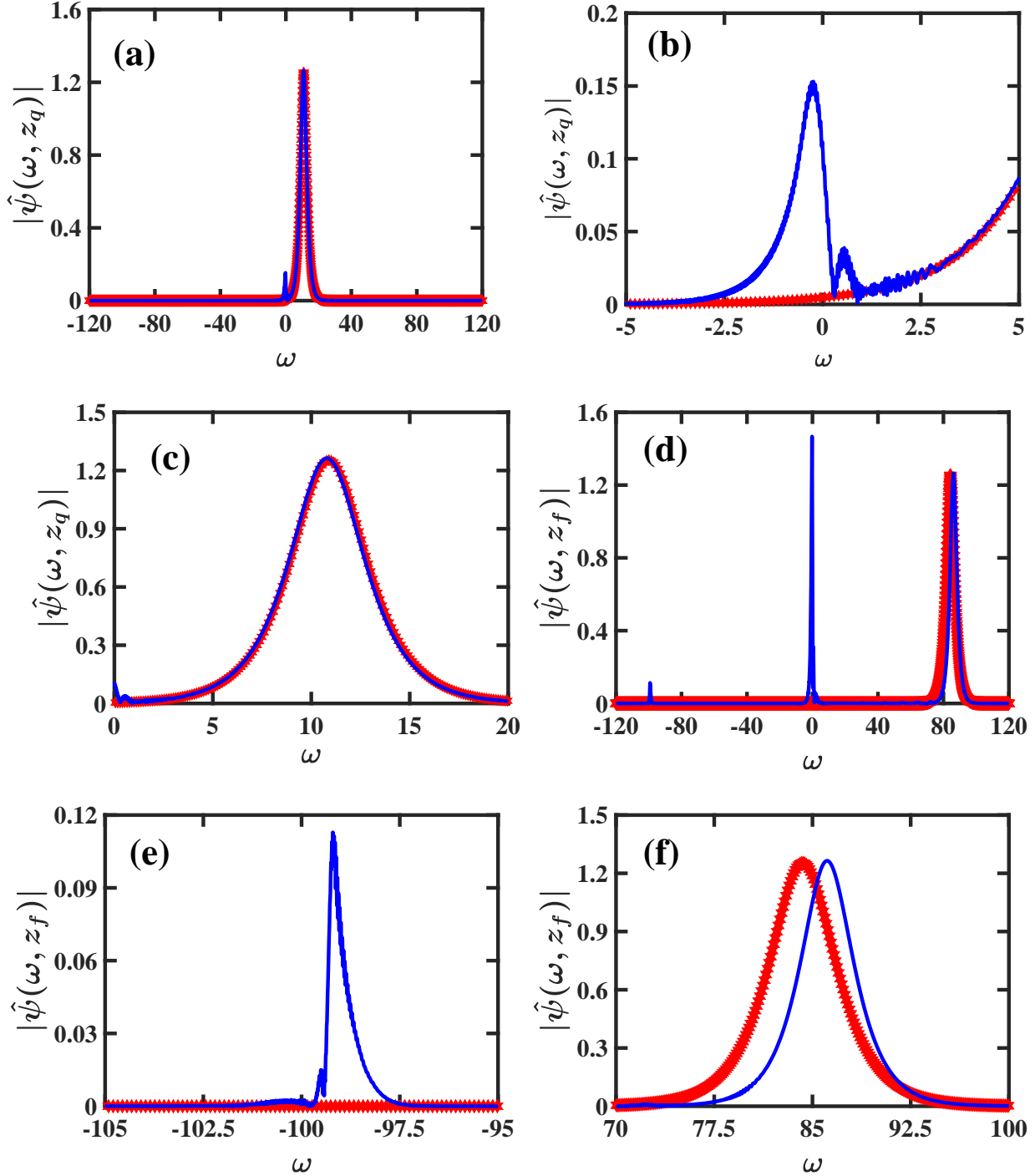


FIG. 7: The shape of the Fourier spectrum $|\hat{\psi}(\omega, z)|$ at $z_q = 20$ [(a), (b), (c)] and at $z_f = 76$ [(d), (e), (f)] for propagation of a CNLS soliton in a waveguide loop with weak frequency-independent linear gain, cubic loss, and delayed Raman response. The parameter values are the same as in Fig. 5. The solid blue curve represents the result obtained by the numerical simulation with Eq. (16), and the red stars correspond to the perturbation theory prediction of Eqs. (B6), (20), and (21).

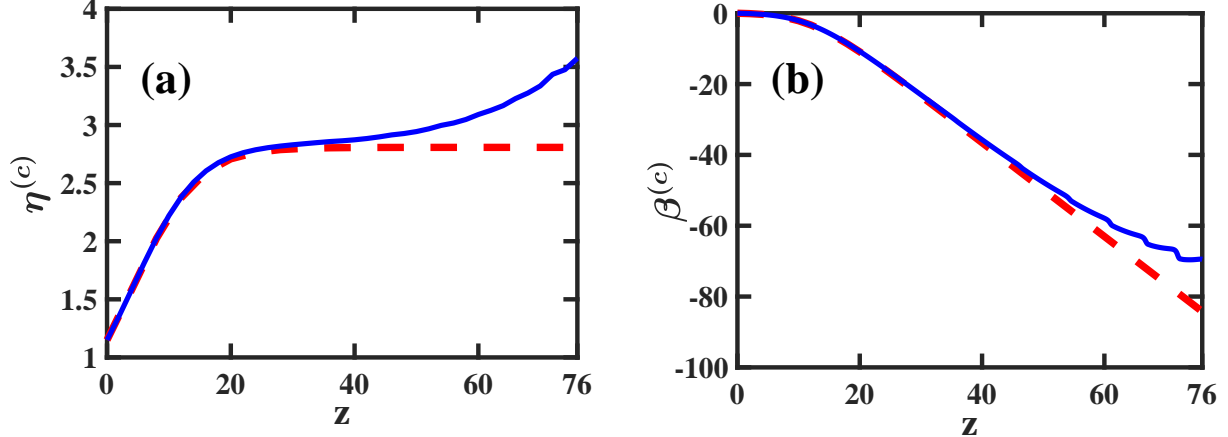


FIG. 8: The z dependence of the CNLS soliton's amplitude $\eta^{(c)}(z)$ (a) and frequency $\beta^{(c)}(z)$ (b) for the waveguide setups considered in Figs. 5-7. The solid blue curves represent the results obtained by numerical solution of Eq. (16). The dashed red curves correspond to the perturbation theory predictions of Eq. (20) in (a) and of Eq. (21) in (b).

sion quality and pulse distortion, are considerably smaller for the CNLS soliton.

2. *Pulse-shape dynamics.* The radiative hump for the CNLS soliton is much more pronounced than the radiative hump for the CQNLS soliton.
3. *The Fourier spectrum.* The Fourier spectrum for the CNLS soliton at $z \leq z_f$ contains pronounced radiative features at high $|\omega|$ values, which are not present in the spectrum for the CQNLS soliton at $z \leq z_f$. In addition, the numerically obtained spectrum of the CNLS soliton at $z = z_f$ is considerably shifted compared with the theoretical prediction, whereas the numerically obtained spectrum of the CQNLS soliton is not.
4. *Amplitude and frequency dynamics.* The deviations of the numerically obtained amplitude and frequency of the soliton from the perturbation theory predictions at distances close or equal to z_f are significantly larger for the CNLS soliton.

Based on these observations, we conclude that transmission instability in waveguide loops with weak frequency-independent linear gain, cubic loss, and delayed Raman response is weaker for the CQNLS soliton than for the CNLS soliton. We also point out that the Raman-induced frequency shift for the CQNLS soliton is much smaller than the frequency shift experienced by the CNLS soliton. This fact combined with the weaker pulse distortion

of the CQNLS soliton indicate that waveguides with focusing cubic nonlinearity and defocusing quintic nonlinearity are advantageous compared with waveguides with focusing cubic nonlinearity for transmission of highly energetic solitons in the presence of weak nonlinear dissipative perturbations.

C. Soliton dynamics in the presence of frequency-dependent linear gain-loss, cubic loss, and delayed Raman response

We now turn to study soliton propagation in nonlinear waveguides with focusing cubic nonlinearity, defocusing quintic nonlinearity, weak frequency-dependent linear gain-loss, cubic loss, and delayed Raman response. Our main goal is to investigate whether the transmission stabilization method that was developed in Ref. [36] for CNLS solitons also works in the nonintegrable case of the CQNLS soliton. Furthermore, we compare the transmission stabilization of the CQNLS soliton with that of the CNLS soliton in the same nonlinear waveguide setup. The propagation of the CQNLS soliton is described by the following perturbed CQNLS equation [62]:

$$i\partial_z\psi + \partial_t^2\psi + 2|\psi|^2\psi - \epsilon_q|\psi|^4\psi = i\mathcal{F}^{-1}(\hat{g}(\omega, z)\hat{\psi})/2 - i\epsilon_3|\psi|^2\psi + \epsilon_R\psi\partial_t|\psi|^2, \quad (22)$$

where ω is angular frequency, $\hat{\psi}$ is the Fourier transform of ψ with respect to time, $\hat{g}(\omega, z)$ is the frequency-dependent linear gain-loss, \mathcal{F}^{-1} is the inverse Fourier transform with respect to time, and the other notations are the same as in Eq. (7).

The form of the frequency and distance-dependent linear gain-loss $\hat{g}(\omega, z)$ is chosen such that radiation emission effects are mitigated, soliton shape is retained, and the value of the amplitude parameter η approaches the desired equilibrium value η_0 . More specifically, we choose the form

$$\begin{aligned} \hat{g}(\omega, z) = & -g_L + \frac{1}{2}(g_0 + g_L)[\tanh\{\rho[\omega + \beta(z) + W/2]\} \\ & - \tanh\{\rho[\omega + \beta(z) - W/2]\}], \end{aligned} \quad (23)$$

where g_0 is the linear gain coefficient, $\beta(z)$ is the soliton frequency at distance z , g_L is an $O(1)$ positive constant, and g_0 , W , and ρ satisfy $0 < g_0 \ll 1$, $W \gg 1$, and $\rho \gg 1$. The form (23) is similar to the one used in Ref. [36] for stabilization of the CNLS soliton, and also to the form used in Refs. [37–39] in studies of multisequence transmission of CNLS solitons in

the presence of various weak dissipative nonlinear perturbations. Since $\rho \gg 1$, $\hat{g}(\omega, z)$ can be approximated by the following step function:

$$\hat{g}(\omega, z) \simeq \begin{cases} g_0 & \text{if } -\beta(z) - W/2 < \omega < -\beta(z) + W/2, \\ (g_0 - g_L)/2 & \text{if } \omega = -\beta(z) - W/2 \text{ or } \omega = -\beta(z) + W/2, \\ -g_L & \text{elsewhere.} \end{cases} \quad (24)$$

We point out that the constant weak linear gain g_0 in the frequency interval $(-\beta(z) - W/2, -\beta(z) + W/2)$ balances the effects of the weak cubic loss, such that the soliton amplitude approaches the equilibrium value η_0 with increasing distance. Additionally, the strong linear loss $-g_L$ suppresses emission of radiation with frequencies outside of the interval $(-\beta(z) - W/2, -\beta(z) + W/2)$. Furthermore, the Raman perturbation is expected to generate a relatively large separation between the soliton's spectrum and the radiation's spectrum. As a result, the introduction of the frequency-dependent linear gain-loss $\hat{g}(\omega, z)$ is expected to lead to efficient suppression of pulse-shape distortion and to significant enhancement of transmission stability. We also note that the flat gain in the interval $(-\beta(z) - W/2, -\beta(z) + W/2)$ can be realized by flat-gain amplifiers [71], and the strong loss outside of this interval can be achieved by filters [71] or by waveguide impurities [4].

Using an energy balance calculation, we show in Appendix A that the dynamics of the soliton's amplitude is described by

$$\frac{d\eta}{dz} = \frac{(\eta_m^2 - \eta^2)}{\eta_m} \left\{ -g_L \operatorname{arctanh} \left(\frac{\eta}{\eta_m} \right) + \frac{(g_0 + g_L)\eta}{\pi\eta_m} J_1(\eta) - 4\epsilon_3 \eta_m^2 \left[\operatorname{arctanh} \left(\frac{\eta}{\eta_m} \right) - \frac{\eta}{\eta_m} \right] \right\}, \quad (25)$$

where

$$J_1(\eta) = \int_{-\infty}^{\infty} ds \frac{\sin(Ws/2)}{s} \int_{-\infty}^{\infty} \frac{dx}{[(1 - \eta^2/\eta_m^2)^{1/2} \cosh(2x) + 1]^{1/2} [(1 - \eta^2/\eta_m^2)^{1/2} \cosh(2x - 2\eta s) + 1]^{1/2}}. \quad (26)$$

Additionally, the modification of the frequency-independent linear gain term of Eq. (7) to the frequency-dependent linear gain-loss term of Eq. (22) does not affect the dynamics of the soliton's frequency in first order in ϵ_R and ϵ_3 . Therefore, the dynamics of β is still given by Eq. (9). As in subsection II B, stable steady-state transmission with constant amplitudes can be realized by requiring that $\eta = \eta_0$ with $0 < \eta_0 < \eta_m$ is a stable equilibrium point of

Eq. (25). This requirement yields the following expression for g_0 :

$$g_0 = -g_L + \frac{\pi\eta_m}{\eta_0 J_1(\eta_0)} \left\{ g_L \operatorname{arctanh} \left(\frac{\eta_0}{\eta_m} \right) + 4\epsilon_3 \eta_m^2 \left[\operatorname{arctanh} \left(\frac{\eta_0}{\eta_m} \right) - \frac{\eta_0}{\eta_m} \right] \right\}. \quad (27)$$

Thus, the complete description of amplitude dynamics subject to the requirement on η_0 is given by Eqs. (25), (26), and (27). Furthermore, using Eq. (27), we can write the equation for the dynamics of η in the form

$$\frac{d\eta}{dz} = \left(1 - \frac{\eta^2}{\eta_m^2} \right) \eta \tilde{J}_1 \left(\frac{\eta}{\eta_m} \right) \left[G \left(\frac{\eta}{\eta_m} \right) - G \left(\frac{\eta_0}{\eta_m} \right) \right], \quad (28)$$

where $\tilde{J}_1(\eta/\eta_m) = J_1(\eta)$, and

$$G(x) = \frac{1}{x \tilde{J}_1(x)} \left\{ 4\epsilon_3 \eta_m^2 [x - \operatorname{arctanh}(x)] - g_L \operatorname{arctanh}(x) \right\}. \quad (29)$$

It is possible to show that $\eta = \eta_0$ is the only equilibrium point of Eq. (28) with a nonnegative amplitude value and that it is a stable equilibrium point for a range of physical parameter values, including the values considered in the current paper.

Let us discuss the approximate form of the equations for $d\eta/dz$ and $d\beta/dz$ in the following two cases that were also considered in subsection II B. (1) The limit $\epsilon_q \rightarrow 0^+$ ($\eta_m \rightarrow \infty$) that corresponds to the CNLS limit. (2) The case where η is close to η_0 , and η_0 is close to η_m (that is, for highly energetic CQNLS solitons near the flat-top soliton limit). In the limit $\epsilon_q \rightarrow 0^+$, we retrieve the equations for the dynamics of the CNLS soliton's amplitude and frequency that were obtained in Ref. [36]. More specifically, we obtain

$$\frac{d\eta}{dz} \simeq \left\{ g_L \left[\frac{\tanh(V)}{\tanh(V_0)} - 1 \right] + \frac{4}{3} \epsilon_3 \left[\eta_0^2 \frac{\tanh(V)}{\tanh(V_0)} - \eta^2 \right] \right\} \eta, \quad (30)$$

where $V = \pi W/(4\eta)$ and $V_0 = \pi W/(4\eta_0)$. Additionally, since the dynamics of β is described by Eq. (9), the approximate form of this equation in the limit $\epsilon_q \rightarrow 0^+$ is still given by Eq. (13). In case (2), we linearize Eq. (28) about $\eta = \eta_0$, and obtain

$$\begin{aligned} \frac{d\eta}{dz} \simeq & \left\{ -(12\epsilon_3 \eta_0^2 + g_L) + 2 \left(4\epsilon_3 \eta_m + \frac{g_L}{\eta_m} \right) \operatorname{arctanh}(\eta_0/\eta_m) \right. \\ & \left. - \frac{G(\eta_0/\eta_m)}{\eta_m^2} \left[(\eta_m^2 - 3\eta_0^2) J_1(\eta_0) + (\eta_m^2 - \eta_0^2) \eta_0 J'_1(\eta_0) \right] \right\} \delta\eta, \end{aligned} \quad (31)$$

where $\delta\eta = \eta - \eta_0$. In addition, in this case, the approximate form of the equation for β is given by Eq. (15).

Numerical simulations. The prediction for enhanced stability of the CQNLS soliton due to the interplay between frequency-dependent linear gain-loss and the Raman-induced

self-frequency shift is based on a heuristic argument. It is therefore important to check the validity of this prediction by numerical simulations with Eqs. (22) and (23). To enable comparison with the simulations results of Sec. II B, we use a simulation setup that is similar to the one used in Sec. II B. More specifically, we solve Eqs. (22) and (23) numerically on a time domain $[t_{\min}, t_{\max}] = [-400, 400]$ with the split-step method and with periodic boundary conditions. Since we use periodic boundary conditions, the simulation describes propagation in a closed waveguide loop. Therefore, the simulation and the analysis are highly relevant for most long-distance optical waveguide transmission experiments, which are carried out in closed loops [41, 42, 66–68]. The initial condition is in the form of the CQNLS soliton of Eq. (2) with parameter values $\eta(0), \beta(0) = 0, y(0) = 0$, and $\alpha(0) = 0$. The comparison with the results of Sec. II B is facilitated by choosing similar parameter values to the ones used in that section. That is, we consider here the results of the simulation with $\epsilon_q = 0.5, \epsilon_3 = 0.01, \epsilon_R = 0.04, \eta_0 = 1.2$, and $\eta(0) = 0.9$. Since $\eta_0 = 1.2$ is close to $\eta_m = 1.2247\dots$, we are in fact considering transmission stabilization of highly energetic solitons near the flat-top soliton limit. The values of the parameters W, ρ , and g_L in Eq. (23) are the same as the values used in Refs. [36–39] in studies of stabilization of CNLS solitons with different perturbed CNLS and coupled-CNLS models: $W = 10, \rho = 10$, and $g_L = 0.5$. We point out that numerical simulations with other values of the physical parameters yield similar results. We run the simulation up to a final distance $z_f = 2000$, and check if the value of the transmission quality integral $I(z)$ remains smaller than 0.075 throughout the simulation.

Figure 9 shows the numerical simulation’s result for the pulse shape $|\psi(t, z)|$ at $z = z_f$ together with the perturbation theory prediction of Eqs. (B1) and (28). We observe that the numerically obtained pulse shape at $z = z_f$ is very close to the theoretical prediction and no appreciable pulse distortion due to radiation emission is present [see Figs. 9(a) and 9(b)]. Furthermore, as seen in Fig. 9(c), the deviation of the simulation’s result from the theoretical prediction at $z = z_f$ is smaller than 10^{-6} for all t values. Surprisingly, this deviation is of the same order of magnitude as the deviation observed in Ref. [36] for a CNLS soliton with an equilibrium power value that is smaller than the CQNLS soliton’s equilibrium power in the current simulation by a factor of 2.8086. The enhanced transmission stability of the CQNLS soliton is also clearly visible in Fig. 10, which shows the numerically obtained $I(z)$ curve. As seen in this figure, the value of $I(z)$ is smaller than 0.053 throughout the

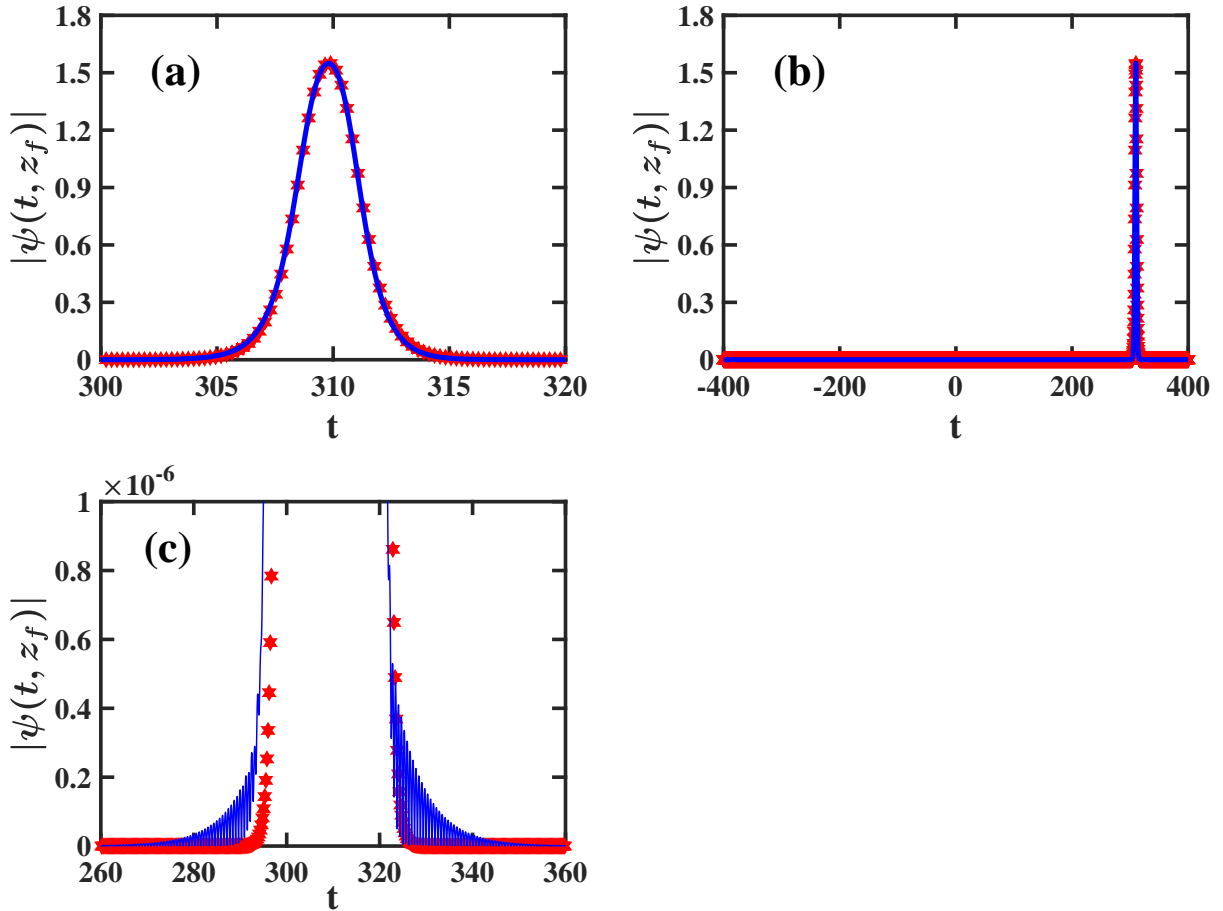


FIG. 9: The pulse shape $|\psi(t, z_f)|$, where $z_f = 2000$, for propagation of a CQNLS soliton in a waveguide loop with weak frequency-dependent linear gain-loss, cubic loss, and delayed Raman response. The physical parameter values are $\epsilon_q = 0.5$, $\epsilon_3 = 0.01$, $\epsilon_R = 0.04$, $\eta_0 = 1.2$, $\eta(0) = 0.9$, $W = 10$, $\rho = 10$, and $g_L = 0.5$. The solid blue curve corresponds to the result obtained by the numerical simulation with Eqs. (22) and (23). The red stars represent the perturbation theory prediction of Eqs. (B1) and (28).

propagation. Additionally, the average $\langle I(z) \rangle$, which is defined by $\langle I(z) \rangle \equiv \int_0^{z_f} dz' I(z')/z_f$, is $\langle I(z) \rangle = 0.02053$, in agreement with the very weak pulse distortion observed in Fig. 9.

Further insight into enhancement of transmission stability is gained by analyzing the Fourier spectrum of the pulse $|\hat{\psi}(\omega, z)|$. Figure 11 shows a comparison between the numerically obtained Fourier spectrum $|\hat{\psi}(\omega, z)|$ at $z = z_f$ and the perturbation theory prediction of Eqs. (B3), (9), and (28). The agreement between the theoretical and the numerical results is excellent. More specifically, the spectrum obtained in the simulation does not

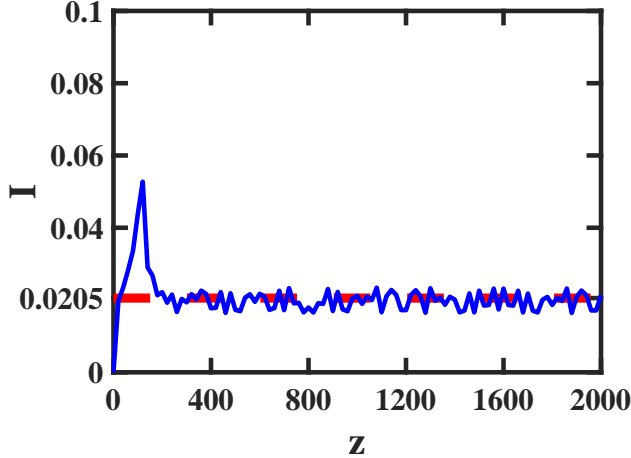


FIG. 10: The z dependence of the transmission quality integral $I(z)$ obtained by the numerical simulation with Eqs. (22) and (23) for the same waveguide setup as in Fig. 9. The solid blue curve represents $I(z)$ and the dashed red horizontal line corresponds to $\langle I(z) \rangle$.

contain any radiative peaks, such as the peaks seen in Figs. 3 and 7. Furthermore, the graph of $|\hat{\psi}(\omega, z_f)|$ vs ω does not contain any significant oscillations, such as the oscillations observed for the CNLS soliton in the absence of perturbation-induced frequency shifting in Ref. [36]. These findings together with the findings in Sec. II B show that the interplay between perturbation-induced shifting of the soliton's frequency and frequency-dependent linear gain-loss indeed leads to enhanced transmission stability of the CQNLs soliton, and that it does so even for highly energetic CQNLs solitons near the flat-top soliton limit. Thus, the stabilization method that was developed in Ref. [36] for solitons of the integrable CNLS equation also works for solitons of the nonintegrable CQNLs equation far from the CNLS limit. Transmission stabilization takes place in the following manner. The perturbation-induced frequency shift experienced by the soliton (due to the Raman effect, for example) leads to the separation of the soliton's spectrum from the radiation's spectrum, while the frequency-dependent linear gain-loss leads to efficient suppression of the emitted radiation.

The enhanced transmission stability in waveguides with frequency-dependent linear gain-loss and delayed Raman response has important consequences for the dynamics of the CQNLs soliton's amplitude and frequency. Figure 12 shows the z dependence of the soliton's amplitude and frequency obtained by numerical solution of Eqs. (22) and (23) along with the perturbation theory predictions of Eqs. (28) and (9). The agreement between the perturbation theory predictions and the simulation's results is excellent. In particular,

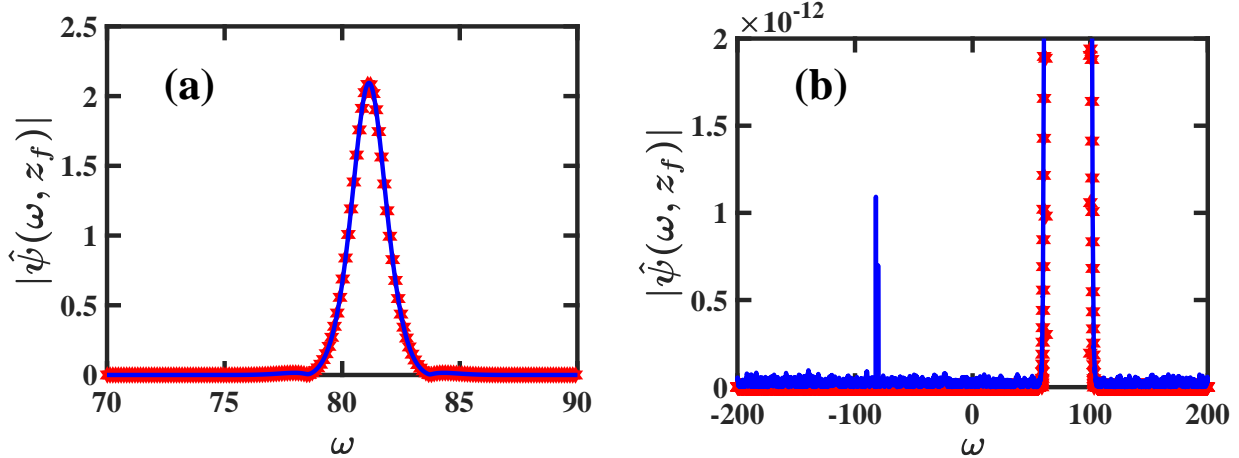


FIG. 11: The shape of the Fourier spectrum $|\hat{\psi}(\omega, z_f)|$, where $z_f = 2000$, for propagation of a CQNLS soliton in a waveguide loop with weak frequency-dependent linear gain-loss, cubic loss, and delayed Raman response. The parameter values are the same as in Fig. 9. The solid blue curve represents the result obtained by numerical solution of Eqs. (22) and (23), and the red stars correspond to the perturbation theory prediction of Eqs. (B3), (9), and (28).

the numerically obtained amplitude value tends to the equilibrium value $\eta_0 = 1.2$ at short distances and continues to be close to this value throughout the propagation, in very good agreement with the theoretical prediction. In addition, the numerically obtained value of the soliton's frequency stays close to the z -dependent value predicted by Eqs. (9) and (28). Therefore, the efficient suppression of radiation emission and the enhanced stability of the CQNLS soliton in waveguides with weak frequency-dependent linear gain-loss, cubic loss, and delayed Raman response enable observation of stable amplitude and frequency dynamics along significantly larger distances compared with the distances obtained with the waveguide setups of section II B, which relied on weak frequency-independent linear gain.

Comparison with transmission stability of the CNLS soliton. Let us compare the results of the numerical simulation for transmission stabilization of the CQNLS soliton with the results of simulations for transmission stabilization of the CNLS soliton in the same optical waveguide setup. This comparison is very useful in determining whether the presence of defocusing quintic nonlinearity improves the transmission stabilization method that is based on the interplay between perturbation-induced frequency shifting and frequency-dependent linear gain-loss. The comparison is realized by performing numerical simulations with the

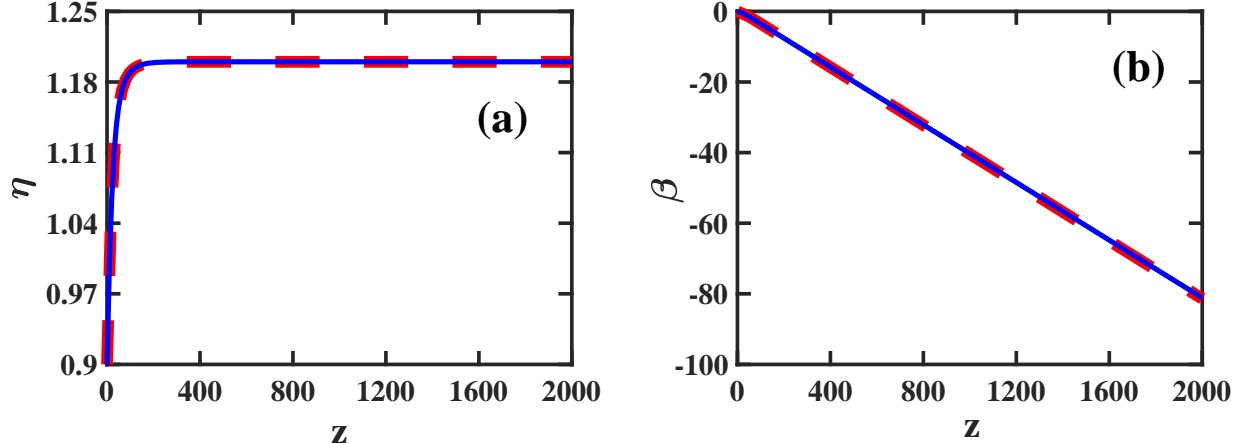


FIG. 12: The z dependence of the CQNLS soliton's amplitude $\eta(z)$ (a) and frequency $\beta(z)$ (b) for the same waveguide setup as in Figs. 9-11. The solid blue curves represent the results obtained by numerical solution of Eqs. (22) and (23). The dashed red curves correspond to the perturbation theory predictions of Eq. (28) in (a), and of Eqs. (9) and (28) in (b).

following perturbed CNLS model [36]:

$$i\partial_z\psi + \partial_t^2\psi + 2|\psi|^2\psi = i\mathcal{F}^{-1}(\hat{g}(\omega, z)\hat{\psi})/2 - i\epsilon_3|\psi|^2\psi + \epsilon_R\psi\partial_t|\psi|^2, \quad (32)$$

where $\hat{g}(\omega, z)$ is given by Eq. (23). Note that Eq. (32) is just Eq. (22) without the quintic nonlinearity term. The initial condition for the simulation is in the form of the fundamental CNLS soliton (17). In Ref. [36], we used the adiabatic perturbation theory for the CNLS soliton to show that the dynamics of its amplitude is described by

$$\frac{d\eta^{(c)}}{dz} = \left\{ g_L \left[\frac{\tanh(V^{(c)})}{\tanh(V_0^{(c)})} - 1 \right] + \frac{4}{3}\epsilon_3 \left[\eta_0^{(c)2} \frac{\tanh(V^{(c)})}{\tanh(V_0^{(c)})} - \eta^{(c)2} \right] \right\} \eta^{(c)}, \quad (33)$$

where $V^{(c)} = \pi W/(4\eta^{(c)})$, $V_0^{(c)} = \pi W/(4\eta_0^{(c)})$, and

$$g_0 = -g_L + \frac{\left(g_L + 4\epsilon_3\eta_0^{(c)2}/3 \right)}{\tanh(V_0^{(c)})}. \quad (34)$$

Additionally, the dynamics of the soliton's frequency is still given by Eq. (19). It was shown in Ref. [36] that $\eta^{(c)} = \eta_0^{(c)}$ is the only equilibrium point of Eq. (33) with a nonnegative amplitude value and that it is a stable equilibrium point.

We solve Eqs. (32) and (23) numerically on a time domain $[t_{\min}, t_{\max}] = [-400, 400]$ with periodic boundary conditions, and with the initial condition (17) with parameter values $\eta^{(c)}(0)$, $\beta^{(c)}(0) = 0$, $y^{(c)}(0) = 0$, and $\alpha^{(c)}(0) = 0$. To enable a fair comparison with

stabilization of the CQNLS soliton, we use the same parameter values that were used in the simulation with the perturbed CQNLS model (22), i.e., $\epsilon_3 = 0.01$, $\epsilon_R = 0.04$, $W = 10$, $\rho = 10$, and $g_L = 0.5$. Additionally, we require that the initial power and the equilibrium power of the CNLS soliton would be equal to the initial power and the equilibrium power of the CQNLS soliton. Therefore, the values of $\eta_0^{(c)}$ and $\eta^{(c)}(0)$ used in the simulation with Eqs. (32) and (23) are $\eta_0^{(c)} = 2.8086\dots$ and $\eta^{(c)}(0) = 1.1503\dots$. Due to the large frequency shift experienced by the CNLS soliton, we must employ a larger frequency domain, and smaller time and distance steps. As a result, the largest value of z_f that can be used with a reasonable computation time is restricted to $z_f \simeq 200$ [72]. Therefore, we run the simulation up to the final distance $z_f = 200$.

The numerical simulation's result for the pulse shape $|\psi(t, z)|$ at $z = z_f = 200$ is shown in Fig. 13 together with the theoretical prediction of Eqs. (B5) and (33). As seen in Figs. 13(a) and 13(b), the numerically obtained pulse shape at $z = z_f$ is close to the theoretical prediction and no significant radiation-induced pulse distortion is found. However, the comparison in Figs. 13(c) and 13(d) for small $|\psi(t, z_f)|$ values reveals the presence of a small radiative tail and weak pulse distortion, which leads to an order 10^{-4} deviation of the numerical result from the theoretical prediction. This deviation is larger by 2 orders of magnitude compared with the deviation found for the CQNLS soliton at $z_f = 2000$ in the same waveguide setup [see Fig. 9(c)]. On the other hand, the deviation is significantly smaller than the order 0.1 deviation observed for the CNLS soliton at $z_f = 76$ in waveguides with frequency-independent linear gain [see Fig. 5(f)]. The latter comparison indicates that transmission of energetic CNLS solitons in waveguides with weak frequency-dependent linear gain-loss and delayed Raman response is stable. However, due to the relatively small value of z_f in the current simulation, further numerical simulations with more powerful computers are required for verifying this conclusion. The conclusion about transmission stability of the CNLS soliton is also supported by the $I(z)$ curve for the numerical simulation, which is shown in Fig. 14. As seen in this figure, the value of $I(z)$ remains smaller than 0.059 throughout the propagation, and $\langle I(z) \rangle = 0.04855$. Note that the value of $\langle I(z) \rangle$ is larger by a factor of 2.4 compared with the corresponding value for the CQNLS soliton, in accordance with the stronger pulse distortion experienced by the CNLS soliton.

Further understanding of transmission stabilization of the CNLS soliton can be gained by analyzing the Fourier spectrum of the pulse. A comparison between the simulation's result

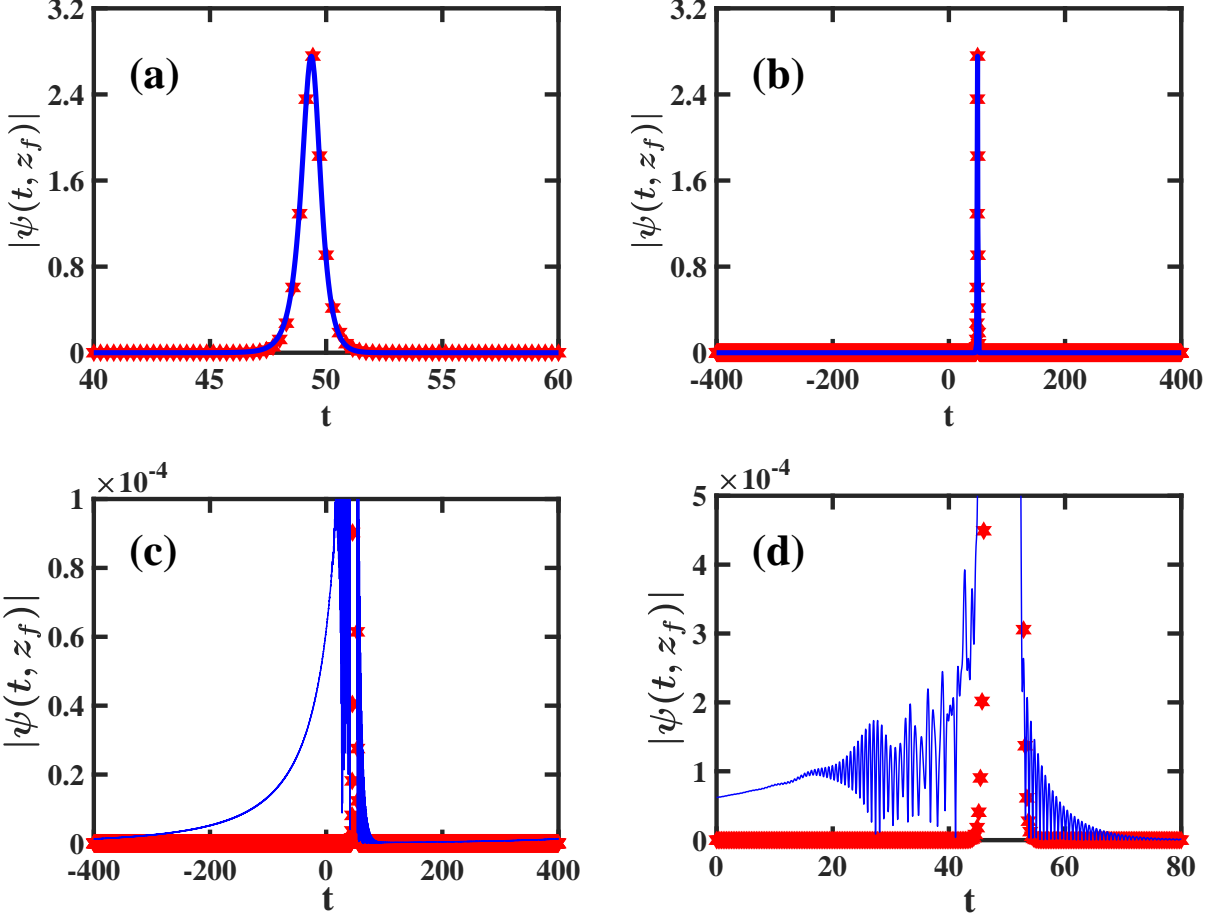


FIG. 13: The pulse shape $|\psi(t, z_f)|$, where $z_f = 200$, for propagation of a CNLS soliton in a waveguide loop with weak frequency-dependent linear gain-loss, cubic loss, and delayed Raman response. The parameter values are $\epsilon_q = 0.5$, $\epsilon_3 = 0.01$, $\epsilon_R = 0.04$, $\eta_0^{(c)} = 2.8086\dots$, $\eta^{(c)}(0) = 1.1503\dots$, $W = 10$, $\rho = 10$, and $g_L = 0.5$. The solid blue curve corresponds to the result obtained by the numerical simulation with Eqs. (32) and (23). The red stars represent the perturbation theory prediction of Eqs. (B5) and (33).

for the Fourier spectrum $|\hat{\psi}(\omega, z)|$ at $z = z_f = 200$ and the perturbation theory prediction of Eqs. (B6), (19), and (33) is shown in Fig. 15. As seen in Fig. 15(a), the agreement between the numerical and the theoretical results is very good and no significant radiative peaks are present. Additionally, the comparison in Figs. 15(b) and 15(c) reveals the existence of a weak oscillatory distortion at the low frequency tail of the soliton's spectrum. This distortion leads to an order 10^{-5} deviation of the numerically obtained spectrum from the theoretical prediction. However, the latter deviation is significantly smaller than the order 1

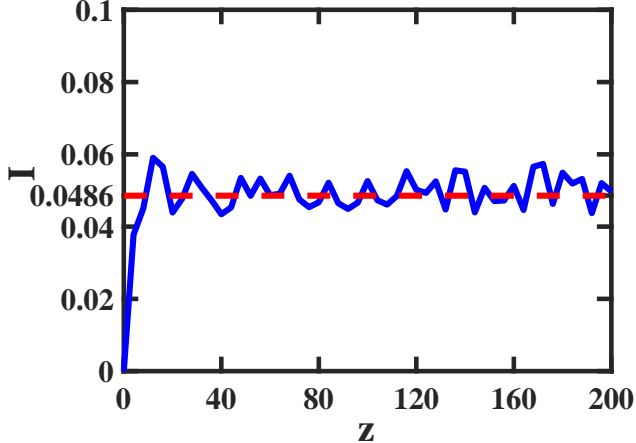


FIG. 14: The z dependence of the transmission quality integral $I(z)$ obtained by the numerical simulation with Eqs. (32) and (23) for the same waveguide setup as in Fig. 13. The solid blue curve represents $I(z)$ and the dashed red horizontal line represents $\langle I(z) \rangle$.

deviation that is found for the CNLS soliton at $z_f = 76$ in waveguides with weak frequency-independent linear gain [see Fig. 7(d)]. Therefore, the results shown in Fig. 15 support our conclusion from Figs. 13 and 14 about transmission stability of the CNLS soliton in waveguides with weak frequency-dependent linear gain-loss, cubic loss, and delayed Raman response.

The suppression of pulse distortion for the CNLS soliton that is observed in Figs. 13-15 has important implications for the dynamics of the soliton's amplitude and frequency. The z dependence of the soliton's amplitude and frequency obtained by numerical solution of Eqs. (32) and (23) is shown in Fig. 16 together with the perturbation theory predictions of Eqs. (33) and (19). The agreement between the theoretical predictions and the simulation's results is very good. More specifically, the value of the soliton's amplitude obtained in the simulation tends to the equilibrium value $\eta_0^{(c)} = 2.8086\dots$ at short distances and stays close to this value throughout the simulation, in full accordance with the theoretical prediction. Furthermore, the numerically obtained value of the soliton's frequency remains close to the z -dependent value predicted by the perturbation theory. Therefore, the results shown in Fig. 16 support our conclusion that transmission of the CNLS soliton in waveguides with weak frequency-dependent linear gain-loss, cubic loss, and delayed Raman response is stable despite the relatively large value of $\eta_0^{(c)}$. Nevertheless, due to the relatively small z_f value in the current numerical simulation, additional simulations are needed for verifying the

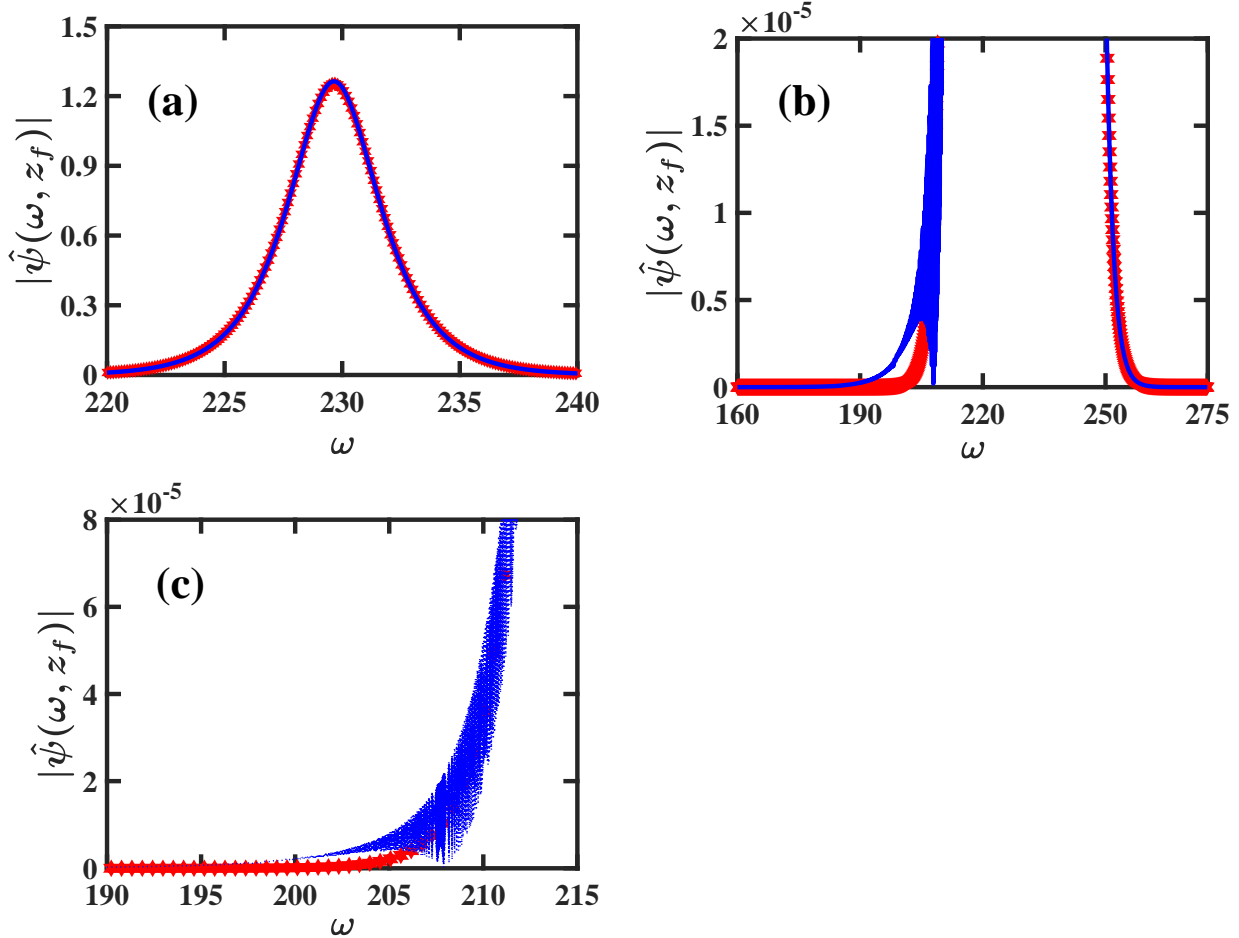


FIG. 15: The shape of the Fourier spectrum $|\hat{\psi}(\omega, z_f)|$, where $z_f = 200$, for propagation of a CNLS soliton in a waveguide loop with weak frequency-dependent linear gain-loss, cubic loss, and delayed Raman response. The parameter values are the same as in Fig. 13. The solid blue curve represents the result obtained by numerical solution of Eqs. (32) and (23), and the red stars represent the perturbation theory prediction of Eqs. (B6), (19), and (33).

conclusion.

Summary. The comparison between Figs. 9-12 and Figs. 13-16 shows that enhancement of transmission stability is stronger for the CQNLs soliton than for the CNLS soliton. In particular, the distortion of the pulse shape, the average value of $I(z)$, and the distortion of the Fourier spectrum are significantly smaller for the CQNLs soliton. Furthermore, the Raman-induced frequency shift is remarkably smaller for the CQNLs soliton [compare Figs. 12(b) and 16(b)]. Based on these findings, we conclude that transmission stabilization of

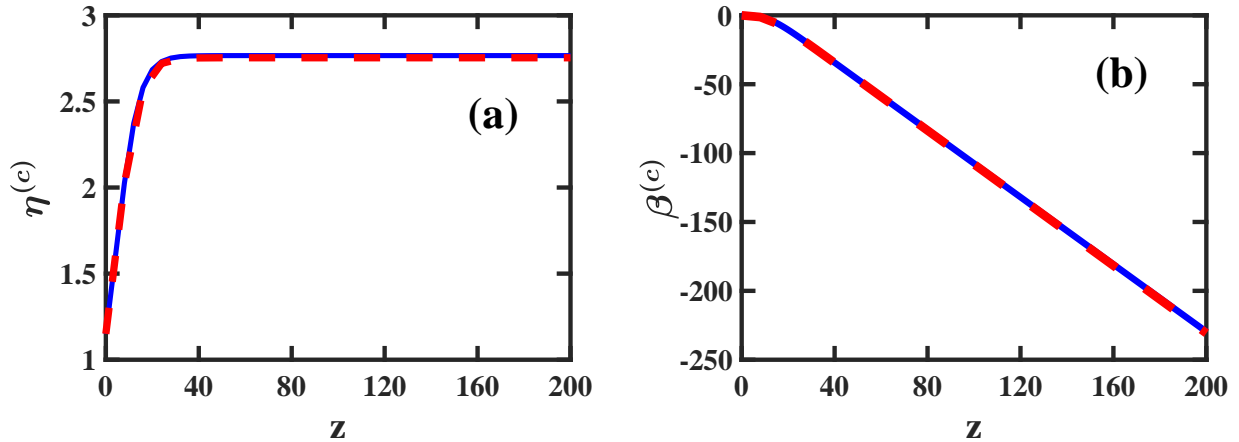


FIG. 16: The z dependence of the CNLS soliton's amplitude $\eta^{(c)}(z)$ (a) and frequency $\beta^{(c)}(z)$ (b) for the waveguide setups considered in Figs. 13-15. The solid blue curves represent the results obtained by numerical solution of Eqs. (32) and (23). The dashed red curves correspond to the perturbation theory predictions of Eq. (33) in (a), and of Eqs. (19) and (33) in (b).

highly energetic solitons by frequency-dependent linear gain-loss and perturbation-induced frequency shifting is much more robust in waveguides with focusing cubic nonlinearity and defocusing quintic nonlinearity than in waveguides with focusing cubic nonlinearity.

III. CONCLUSIONS

We demonstrated stabilization of energetic solitons of the nonintegrable CQNLS equation by a method that is based on the interplay between perturbation-induced shifting of the soliton's frequency and frequency-dependent linear gain-loss. The method was developed and demonstrated in Ref. [36] for solitons of the integrable CNLS equation. However, it is unclear if the method works for nonintegrable nonlinear wave models far from their integrable limit. Furthermore, it is unclear whether soliton stability is enhanced or reduced in the nonintegrable case compared with the integrable one. In the current work, we addressed these important questions by considering the propagation of a highly energetic CQNLS soliton in a nonlinear optical waveguide with focusing cubic nonlinearity, defocusing quintic nonlinearity, and three weak perturbations due to weak linear gain-loss, cubic loss, and delayed Raman response. In this system, the weak linear gain-loss counteracts the effects of weak cubic loss, such that the value of the soliton's amplitude tends to an equilibrium value.

Additionally, the shifting of the soliton's frequency is caused by the Raman perturbation. We considered two different waveguide setups, one with frequency-independent linear gain, and another with frequency-dependent linear gain-loss. For each waveguide setup, we used perturbative calculations to derive equations for the dynamics of the CQNLS soliton's amplitude and frequency in the presence of the three perturbations. Furthermore, we carried out numerical simulations with the perturbed CQNLS equation and characterized the distortion of the pulse shape and the Fourier spectrum. We also compared the simulations results with results of numerical simulations for propagation of a highly energetic CNLS soliton in similar waveguide setups in the absence of quintic nonlinearity.

In the case of waveguides with frequency-independent linear gain, our numerical simulations showed that transmission of the CQNLS soliton becomes unstable due to radiation emission effects. The radiation emitted by the soliton forms a highly oscillatory hump, which is spread over the entire computational domain. Additionally, the soliton's and radiation's Fourier spectra become separated due to the Raman-induced frequency shift of the CQNLS soliton. However, the presence of frequency-independent linear gain leads to continued growth of the radiation. As a result, the radiative hump continues to grow with increasing distance and the transmission becomes unstable. An important consequence of this radiative instability is that the numerically obtained values of the CQNLS soliton's amplitude and frequency deviate from the perturbation theory predictions at intermediate distances, i.e., the dynamics of the soliton's parameters is also unstable. A comparison with results of numerical simulations with the perturbed CNLS equation for soliton propagation in a similar waveguide setup showed that transmission instability is stronger for the CNLS soliton. We also found that the Raman-induced frequency shift is significantly larger for the CNLS soliton. Thus, our results indicated that transmission of highly energetic CQNLS solitons in the presence of weak nonlinear dissipative perturbations is advantageous compared with transmission of highly energetic CNLS solitons in the presence of the same dissipative perturbations.

Remarkable enhancement of transmission stability of the CQNLS soliton was realized in waveguides with frequency-dependent linear gain-loss. In this case, our numerical simulations showed that the pulse distortion experienced by the soliton is extremely small (of order 10^{-6} or smaller). Surprisingly, this pulse distortion is of the same order of magnitude as the pulse distortion observed in Ref. [36] for CNLS solitons with a significantly smaller

equilibrium power value. The enhanced transmission stability of the CQNLS soliton was also manifested in the dynamics of its amplitude and frequency. Indeed, the numerically obtained amplitude and frequency exhibited stable dynamics throughout the long-haul propagation (over a distance $z_f = 2000$), in excellent agreement with the perturbation theory predictions. Further numerical simulations for propagation of a CNLS soliton in waveguides with frequency-dependent linear gain-loss indicated that the transmission is stable in this case as well. However, due to the large Raman-induced frequency shift experienced by the CNLS soliton, the CNLS simulations were run up to the relatively small final distance $z_f = 200$. The pulse distortion of the CNLS soliton was significantly larger than the pulse distortion of the CQNLS soliton in the same waveguide setup, but considerably smaller than the distortion of the CNLS soliton in waveguides with frequency-independent linear gain. Based on these results, we concluded that transmission stabilization of highly energetic solitons by frequency-dependent linear gain-loss and perturbation-induced frequency shifting is much more robust in waveguides with focusing cubic nonlinearity and defocusing quintic nonlinearity than in waveguides with focusing cubic nonlinearity.

In summary, we demonstrated that the transmission stabilization method that was developed in Ref. [36] for solitons of the CNLS equation also works for highly energetic solitons of the CQNLS equation far from the CNLS limit. The method is based on the interplay between perturbation-induced shifting of the soliton's frequency and frequency-dependent linear gain-loss. Our numerical simulations and perturbation analysis showed that the frequency shifting experienced by the CQNLS soliton (due to delayed Raman response in our study) indeed leads to a separation of its Fourier spectrum from the radiation's Fourier spectrum, while the frequency-dependent linear gain-loss leads to efficient suppression of radiation emission. As a result, we observed stable long-distance propagation of the highly energetic CQNLS soliton with almost no pulse distortion, and stable dynamics of its amplitude and frequency. Thus, our study provided the first demonstration of the stabilization method for solitons of a nonintegrable nonlinear wave model, far from the integrable limit.

Appendix A: Derivation of the equations for amplitude and frequency dynamics

In this appendix, we derive Eqs. (8), (9), and (25), for the dynamics of the CQNLS soliton's amplitude and frequency in the presence of weak linear gain-loss, cubic loss, and

delayed Raman response. The derivation is based on energy and momentum balance calculations that use the expressions for the power \mathcal{M} and the momentum \mathcal{P} in Eqs. (4) and (5).

We start by considering the dynamics of the amplitude and frequency parameters of the CQNLS soliton in waveguides with weak frequency-independent linear gain, cubic loss, and delayed Raman response. The propagation is described by the perturbed CQNLS equation (7). We derive the equations for amplitude and frequency dynamics by employing a perturbation theory, which is similar to the adiabatic perturbation theory for the CNLS soliton (see, for example, Refs. [36, 73–76] for a description of the latter theory). We calculate the dynamics in first-order in the two small parameters ϵ_3 and ϵ_R . In our perturbation theory, we write the solution to Eq. (7) in the form

$$\psi(t, z) = \psi_s(t, z) + \psi_{rad}(t, z), \quad (\text{A1})$$

where $\psi_s(t, z)$ is the soliton solution (2) of the unperturbed CQNLS equation with slowly varying parameters, and $\psi_{rad}(t, z)$ is the radiation part, which consists of terms that are proportional to ϵ_3 and ϵ_R . Thus, $\psi_s(t, z)$ in Eq. (A1) is given by:

$$\psi_s(t, z) = \frac{\sqrt{2}\eta(z) \exp[i\chi(t, z)]}{\{[1 - \eta^2(z)/\eta_m^2]^{1/2} \cosh(2x) + 1\}^{1/2}}, \quad (\text{A2})$$

where $x = \eta(z)[t - y(z)]$, $\chi(t, z) = \alpha(z) - \beta(z)[t - y(z)]$, $y(z) = y(0) - 2 \int_0^z dz' \beta(z')$, and $\alpha(z) = \alpha(0) + \int_0^z dz' [\eta^2(z') + \beta^2(z')]$. Employing an energy balance calculation and the ansatz (A1), we find:

$$\partial_z \int_{-\infty}^{\infty} dt |\psi_s(t, z)|^2 = g_0 \int_{-\infty}^{\infty} dt |\psi_s(t, z)|^2 - 2\epsilon_3 \int_{-\infty}^{\infty} dt |\psi_s(t, z)|^4. \quad (\text{A3})$$

We now use the following relations for the two integrals on the right hand side of Eq. (A3) [77]:

$$\int_{-\infty}^{\infty} dt |\psi_s(t, z)|^2 = 2\eta_m \operatorname{arctanh}(\eta/\eta_m), \quad (\text{A4})$$

and

$$\int_{-\infty}^{\infty} dt |\psi_s(t, z)|^4 = 4\eta_m^3 [\operatorname{arctanh}(\eta/\eta_m) - \eta/\eta_m]. \quad (\text{A5})$$

We obtain:

$$\frac{d\eta}{dz} = \frac{(\eta_m^2 - \eta^2)}{\eta_m} \left\{ g_0 \operatorname{arctanh} \left(\frac{\eta}{\eta_m} \right) - 4\epsilon_3 \eta_m^2 \left[\operatorname{arctanh} \left(\frac{\eta}{\eta_m} \right) - \frac{\eta}{\eta_m} \right] \right\}, \quad (\text{A6})$$

which is Eq. (8).

We now turn to derive Eq. (9) for $d\beta/dz$. The derivation is valid for both perturbed CQNLS equations (7) and (22). Within the framework of the first-order perturbation theory, the rate of change of the soliton's momentum is given by

$$\frac{d\mathcal{P}}{dz} \simeq i\partial_z \int_{-\infty}^{\infty} dt [\psi_s(t, z)\partial_t\psi_s^*(t, z) - \psi_s^*(t, z)\partial_t\psi_s(t, z)]. \quad (\text{A7})$$

To obtain the equation for $d\beta/dz$, we derive two different expressions for $d\mathcal{P}/dz$ and equate them. The first expression is obtained by using Eq. (A2) for $\psi_s(t, z)$. The second expression is obtained by using Eq. (7) or Eq. (22) to calculate the right hand side of Eq. (A7).

Using Eq. (A2) for $\psi_s(t, z)$ along with the definition of $\chi(t, z)$, we find: $\partial_t\psi_s = -i\beta\psi_s + \exp(i\chi)\partial_t|\psi_s|$. Substituting this relation and its complex conjugate into Eq. (A7), we arrive at:

$$\frac{d\mathcal{P}}{dz} \simeq -2\frac{d\beta}{dz} \int_{-\infty}^{\infty} dt |\psi_s(t, z)|^2 - 2\beta\partial_z \int_{-\infty}^{\infty} dt |\psi_s(t, z)|^2. \quad (\text{A8})$$

On the other hand, we can express the right hand side of Eq. (A7) in a different manner by performing the differentiation with respect to z inside the integral, and by eliminating the mixed second-order partial derivatives with the help of integration by parts. This calculation yields:

$$\frac{d\mathcal{P}}{dz} \simeq 2i \int_{-\infty}^{\infty} dt [\partial_t\psi_s^*(t, z)\partial_z\psi_s(t, z) - \partial_t\psi_s(t, z)\partial_z\psi_s^*(t, z)]. \quad (\text{A9})$$

We now equate the right hand sides of Eqs. (A8) and (A9), and obtain

$$\begin{aligned} & -\frac{d\beta}{dz} \int_{-\infty}^{\infty} dt |\psi_s(t, z)|^2 - \beta\partial_z \int_{-\infty}^{\infty} dt |\psi_s(t, z)|^2 \\ & = i \int_{-\infty}^{\infty} dt [\partial_t\psi_s^*(t, z)\partial_z\psi_s(t, z) - \partial_t\psi_s(t, z)\partial_z\psi_s^*(t, z)]. \end{aligned} \quad (\text{A10})$$

In the next step, we use Eq. (7) or Eq. (22) to calculate the integral on the right hand side of Eq. (A10). This calculation yields

$$i \int_{-\infty}^{\infty} dt [\partial_t\psi_s^*(t, z)\partial_z\psi_s(t, z) - \partial_t\psi_s(t, z)\partial_z\psi_s^*(t, z)] = \epsilon_R \int_{-\infty}^{\infty} dt [\partial_t|\psi_s(t, z)|^2]^2 + \dots. \quad (\text{A11})$$

The first term on the right hand side of Eq. (A11) is contributed by the delayed Raman response term in Eq. (7) or Eq. (22). The dots represent contributions coming from the gain and loss terms in Eq. (7) or Eq. (22). However, upon substitution of Eq. (A11)

into Eq. (A10), the contributions from the gain and loss terms cancel out with the second term on the left hand side of Eq. (A10). Therefore, we do not write these contributions here explicitly. We now substitute relation (A11) into Eq. (A10), take into account the aforementioned cancellation, and also use relation (A4). We obtain:

$$2\eta_m \operatorname{arctanh} \left(\frac{\eta}{\eta_m} \right) \frac{d\beta}{dz} = -\epsilon_R \int_{-\infty}^{\infty} dt [\partial_t |\psi_s(t, z)|^2]^2. \quad (\text{A12})$$

Using Eq. (A2) for $\psi_s(t, z)$, we can show that

$$\int_{-\infty}^{\infty} dt [\partial_t |\psi_s(t, z)|^2]^2 = 16\eta^5 \left(1 - \frac{\eta^2}{\eta_m^2} \right) \int_{-\infty}^{\infty} dx \frac{\sinh^2(2x)}{[(1 - \eta^2/\eta_m^2)^{1/2} \cosh(2x) + 1]^4}. \quad (\text{A13})$$

The integral on the right hand side of Eq. (A13) can be calculated in a closed form [77]. This calculation yields:

$$\int_{-\infty}^{\infty} dt [\partial_t |\psi_s(t, z)|^2]^2 = \frac{8}{3} \eta_m^5 \left[\frac{3\eta}{\eta_m} - \frac{2\eta^3}{\eta_m^3} - 3 \left(1 - \frac{\eta^2}{\eta_m^2} \right) \operatorname{arctanh} \left(\frac{\eta}{\eta_m} \right) \right]. \quad (\text{A14})$$

Substitution of Eq. (A14) into Eq. (A12) yields the following equation for the dynamics of β :

$$\frac{d\beta}{dz} = \frac{-4\epsilon_R \eta_m^4}{3 \operatorname{arctanh}(\eta/\eta_m)} \left[\frac{3\eta}{\eta_m} - \frac{2\eta^3}{\eta_m^3} - 3 \left(1 - \frac{\eta^2}{\eta_m^2} \right) \operatorname{arctanh} \left(\frac{\eta}{\eta_m} \right) \right]. \quad (\text{A15})$$

Equation (A15) is Eq. (9) of Sec. II B.

Let us derive Eq. (25) for the dynamics of the CQNLS soliton's amplitude in waveguides with weak frequency-dependent linear gain-loss, cubic loss, and delayed Raman response. In this case, the propagation is described by Eq. (22). Applying an energy balance calculation and ansatz (A1), we obtain:

$$\partial_z \int_{-\infty}^{\infty} dt |\psi_s(t, z)|^2 = K_1 + K_1^* - 2\epsilon_3 \int_{-\infty}^{\infty} dt |\psi_s(t, z)|^4, \quad (\text{A16})$$

where

$$K_1 = \frac{1}{2} \int_{-\infty}^{\infty} dt \psi_s^*(t, z) \mathcal{F}^{-1}(\hat{g}(\omega, z) \hat{\psi}_s(\omega, z)). \quad (\text{A17})$$

Using the convolution theorem and Eq. (A2) for $\psi_s(t, z)$, we find

$$K_1 + K_1^* = \frac{\eta(z)}{(2\pi)^{1/2}} \int_{-\infty}^{\infty} \frac{dx}{\{[1 - \eta^2(z)/\eta_m^2]^{1/2} \cosh(2x) + 1\}^{1/2}} \int_{-\infty}^{\infty} ds \frac{\{g(s, z) \exp[i\beta(z)s] + g^*(s, z) \exp[-i\beta(z)s]\}}{\{[1 - \eta^2(z)/\eta_m^2]^{1/2} \cosh[2x - 2\eta(z)s] + 1\}^{1/2}}. \quad (\text{A18})$$

We assume that $\hat{g}(\omega, z)$ can be approximated by Eq. (24). The inverse Fourier transform of the approximate form (24) of $\hat{g}(\omega, z)$ is

$$g(t, z) = -(2\pi)^{1/2} g_L \delta(t) + \left(\frac{2}{\pi}\right)^{1/2} (g_0 + g_L) \exp[-i\beta(z)t] \sin(Wt/2)/t, \quad (\text{A19})$$

where $\delta(t)$ is the Dirac delta function. Substitution of Eq. (A19) into Eq. (A18) yields:

$$K_1 + K_1^* = -2g_L \eta_m \operatorname{arctanh} \left(\frac{\eta}{\eta_m} \right) + \frac{2(g_0 + g_L)\eta}{\pi} J_1(\eta), \quad (\text{A20})$$

where $J_1(\eta)$ is given by Eq. (26). We now substitute Eq. (A20) into Eq. (A16) and also use relation (A5) to calculate the third term on the right hand side of Eq. (A16). We obtain:

$$\begin{aligned} \frac{d\eta}{dz} = & \frac{(\eta_m^2 - \eta^2)}{\eta_m} \left\{ -g_L \operatorname{arctanh} \left(\frac{\eta}{\eta_m} \right) + \frac{(g_0 + g_L)\eta}{\pi \eta_m} J_1(\eta) \right. \\ & \left. - 4\epsilon_3 \eta_m^2 \left[\operatorname{arctanh} \left(\frac{\eta}{\eta_m} \right) - \frac{\eta}{\eta_m} \right] \right\}, \end{aligned} \quad (\text{A21})$$

which is Eq. (25) of Sec. II C.

Appendix B: The transmission quality integral $I(z)$

In this appendix, we present the theoretical predictions for the shape and the Fourier spectrum of the CQNLS and the CNLS solitons, which were used in the analysis of transmission quality and stability. Furthermore, we present the method for calculating the transmission quality integral $I(z)$ and the transmission quality distance z_q from the numerical simulations results.

The theoretical prediction for the shape of the CQNLS soliton is obtained by following the perturbation approach of appendix A. In this approach, we use Eq. (A1) to express the solution of the perturbed CQNLS equation $\psi(t, z)$ as a sum of the soliton part ψ_s and the radiation part ψ_{rad} , where $\psi_s(t, z)$ is defined in Eq. (A2). We therefore take $\psi_s(t, z)$ as the theoretical prediction for the soliton part: $\psi^{(th)}(t, z) \equiv \psi_s(t, z)$. As a result, the theoretical prediction for the shape of the CQNLS soliton is given by:

$$|\psi^{(th)}(t, z)| = \sqrt{2}\eta(z) \left[(1 - \eta(z)^2/\eta_m^2)^{1/2} \cosh(2x) + 1 \right]^{-1/2}, \quad (\text{B1})$$

where $\eta(z)$ is calculated by solving the perturbation theory's equation for $d\eta/dz$, and $y(z)$

is measured from the simulations [78]. The Fourier transform of $\psi_s(t, z)$ with respect to t is

$$\begin{aligned}\hat{\psi}_s(\omega, z) &= \left(\frac{\eta_m}{\pi^2\eta(z)}\right)^{1/2} \Gamma\left(\frac{1}{2} - \frac{i(\omega + \beta(z))}{2\eta(z)}\right) Q_{-\frac{1}{2}}^{\frac{i(\omega + \beta(z))}{2\eta(z)}} \\ &\times \exp\left\{i[\alpha(z) - \omega y(z)] + \frac{\pi(\omega + \beta(z))}{2\eta(z)}\right\},\end{aligned}\quad (\text{B2})$$

where $\Gamma(x)$ is the Gamma function and Q_ν^μ is the associated Legendre function of the second kind [79]. Therefore, the theoretical prediction for the Fourier spectrum of the CQNLS soliton is

$$|\hat{\psi}^{(th)}(\omega, z)| = \left(\frac{\eta_m}{\pi^2\eta(z)}\right)^{1/2} \left|\Gamma\left(\frac{1}{2} - \frac{i(\omega + \beta(z))}{2\eta(z)}\right) Q_{-\frac{1}{2}}^{\frac{i(\omega + \beta(z))}{2\eta(z)}}\right| \exp\left[\frac{\pi(\omega + \beta(z))}{2\eta(z)}\right], \quad (\text{B3})$$

where $\eta(z)$ and $\beta(z)$ are calculated by solving the perturbation theory's equations for $d\eta/dz$ and $d\beta/dz$.

The transmission quality integral measures the deviation of the pulse shape obtained in the simulations $|\psi^{(num)}(t, z)|$ from the soliton's shape predicted by the perturbation theory $|\psi^{(th)}(t, z)|$. We define $I(z)$ in the same manner as we did in previous studies of soliton propagation in nonlinear optical waveguide systems [36, 38]:

$$I(z) = \left[\int_{t_{\min}}^{t_{\max}} dt |\psi^{(th)}(t, z)|^2\right]^{-1/2} \left\{\int_{t_{\min}}^{t_{\max}} dt [\psi^{(th)}(t, z) - \psi^{(num)}(t, z)]^2\right\}^{1/2}, \quad (\text{B4})$$

where the integration is carried out on the entire time domain used in the simulations $[t_{\min}, t_{\max}]$. Note that $I(z)$ measures both distortion in the pulse shape due to radiation emission and deviations of the numerically obtained values of the soliton's parameters from the values predicted by the perturbation theory. Additionally, we define the transmission quality distance z_q as the distance at which the value of $I(z)$ first exceeds a constant value K . In the current paper we use $K = 0.075$. We emphasize, however, that the values of z_q obtained by using this definition are not very sensitive to the value of the constant K . In other words, small changes in the value of K lead to small changes in the measured values of z_q .

The definitions of the theoretical predictions for the shape and the Fourier spectrum of the CNLS soliton are the same as the ones used in Ref. [36]. That is, we use:

$$|\psi^{(c)(th)}(t, z)| = \eta^{(c)}(z) \operatorname{sech} [\eta^{(c)}(z) (t - y^{(c)}(z))], \quad (\text{B5})$$

and

$$|\hat{\psi}^{(c)(th)}(\omega, z)| = \left(\frac{\pi}{2}\right)^{1/2} \operatorname{sech} [\pi (\omega + \beta^{(c)}(z)) / (2\eta^{(c)}(z))], \quad (\text{B6})$$

where $\eta^{(c)}(z)$ and $\beta^{(c)}(z)$ are calculated by the adiabatic perturbation theory for the CNLS soliton, and $y^{(c)}(z)$ is measured from the numerical simulations. The transmission quality integral for the CNLS soliton is calculated by employing Eq. (B4) with $|\psi^{(th)}(t, z)|$ replaced by $|\psi^{(c)(th)}(t, z)|$.

- [1] J. Yang, *Nonlinear Waves in Integrable and Nonintegrable Systems* (SIAM, Philadelphia, 2010).
- [2] G. Fibich, *The Nonlinear Schrödinger Equation, Singular Solutions and Optical Collapse* (Springer, Heidelberg, Germany, 2015).
- [3] D. Pushkarov and S. Tanev, Opt. Commun. **124**, 354 (1996).
- [4] G.P. Agrawal, *Nonlinear Fiber Optics* (Academic, San Diego, CA, 2019).
- [5] L. Gagnon, J. Opt. Soc. Am. A **6**, 1477 (1989).
- [6] Y. Kartashov, V.A. Vysloukh, A.E. Egorov, and A.S. Zelenina, J. Opt. Soc. Am. B **21**, 982 (2004).
- [7] S.J. Shwetanshumala, A. Biswas, and S. Konar, J. Electromagn. Waves and Appl. **20**, 901 (2006).
- [8] K. Senthilnathan, Q. Li, K. Nakkeeran, and P.K.A. Wai, Phys. Rev. A **78**, 033835 (2008).
- [9] E.L. Falcão-Filho, C.B. de Araújo, G. Boudebs, H. Leblond, and V. Skarka, Phys. Rev. Lett. **110**, 013901 (2013).
- [10] R.K. Sarkar and M.K. Dutta, Optik **227**, 166093 (2021).
- [11] D. Mihalache, D. Mazilu, M. Bertolotti, and C. Sibilia, J. Opt. Soc. Am. B **5**, 565 (1988).
- [12] E.B. Kolomeisky, T.J. Newman, J.P. Straley, and X. Qi, Phys. Rev. Lett. **85**, 1146 (2000).
- [13] A. Gammal, T. Frederico, L. Tomio, and P. Chomaz, J. Phys. B **33**, 4053 (2000).
- [14] R. Carretero-González, D.J. Frantzeskakis, and P.G. Kevrekidis, Nonlinearity **21**, R139 (2008).
- [15] E.K. Luckins and R.A. Van Gorder, Ann. Phys. (N. Y.) **388**, 206 (2018).
- [16] C. Zhou, X.T. He, and S. Chen, Phys. Rev. A **46**, 2277 (1992).
- [17] B. Qiao, C.T. Zhou, X.T. He, and C.H. Lai, Commun. Comput. Phys. **4**, 1129 (2008).
- [18] H.D. Singh and B.S. Jatav, Res. Astron. Astrophys. **19**, 93 (2019).
- [19] W. van Saarloos and P.C. Hohenberg, Physica D **56**, 303 (1992).
- [20] I.S. Aranson and L. Kramer, Rev. Mod. Phys. **74**, 99 (2002).

- [21] A. Peleg, T. Dohnal, and Y. Chung, Phys. Rev. E **72**, 027203 (2005).
- [22] A. Peleg, Y. Chung, T. Dohnal, and Q.M. Nguyen, Phys. Rev. E **80**, 026602 (2009).
- [23] D.E. Pelinovsky, Y.S. Kivshar, and V.V. Afanasjev, Physica D **116**, 121 (1998).
- [24] J. Yang and D.J. Kaup, SIAM J. Appl. Math. **60**, 967 (2000).
- [25] Y.S. Kivshar and B.A. Malomed, J. Phys. A **19**, L967 (1986).
- [26] J. Soneson and A. Peleg, Physica D **195**, 123 (2004).
- [27] C. Zhou and X.T. He, Phys. Rev. E **49**, 4417 (1994).
- [28] M. Ohta, Kodai Math. J. **18**, 68 (1995).
- [29] Y. Martel, Probab. Math. Phys. **3**, 839 (2023).
- [30] N. Akhmediev, A. Ankiewicz, and R. Grimshaw, Phys. Rev. E **59**, 6088 (1999).
- [31] R. Carles and C. Sparber, Rev. Math. Phys. **33**, 2150004 (2021).
- [32] T.T. Huynh and Q.M. Nguyen, Appl. Math. Model. **97**, 650 (2021).
- [33] A. Sreedharan, S. Kuriyattil, and S. Wüster, Hyper-entangling mesoscopic bound states, arXiv:2202.06120.
- [34] X.Y. Tang and P.K. Shukla, Phys. Rev. A **76**, 013612 (2007).
- [35] D. Nath, B. Roy, and R. Roychoudhury, Opt. Commun. **393**, 224 (2017).
- [36] A. Peleg and D. Chakraborty, Phys. Rev. A **98**, 013853 (2018).
- [37] D. Chakraborty, A. Peleg, and Q.M. Nguyen, Opt. Commun. **371**, 252 (2016).
- [38] A. Peleg, Q.M. Nguyen, and T.P. Tran, Opt. Commun. **380**, 41 (2016).
- [39] A. Peleg and D. Chakraborty, Commun. Nonlinear Sci. Numer. Simulat. **63**, 145 (2018).
- [40] L.F. Mollenauer, J.P. Gordon, and S.G. Evangelides, Opt. Lett. **17**, 1575 (1992).
- [41] L.F. Mollenauer, J.P. Gordon, and P.V. Mamyshev, in: I.P. Kaminow and T.L. Koch (Eds.), *Optical Fiber Telecommunications III* (Academic, San Diego, CA, 1997), Chapter 12.
- [42] L.F. Mollenauer and J.P. Gordon, *Solitons in Optical Fibers: Fundamentals and Applications* (Academic, San Diego, CA, 2006).
- [43] A. Peleg, Phys. Lett. A **373**, 2734 (2009).
- [44] N.N. Akhmediev and A. Ankiewicz (Eds.), *Dissipative Solitons* (Springer, Berlin, 2005), Chapter 1.
- [45] J.N. Kutz, SIAM Review **48**, 629 (2006).
- [46] Q. Lin, O.J. Painter, and G.P. Agrawal, Opt. Express **15**, 16604 (2007).
- [47] R. Dekker, N. Usechak, M. Först, and A. Driessens, J. Phys. D **40**, R249 (2007).

- [48] M. Borghi, C. Castellan, S. Signorini, A. Trenti, L. Pavesi, *J. Opt.* **19**, 093002 (2017).
- [49] Y.S. Kivshar and B.A. Malomed, *Rev. Mod. Phys.* **61**, 763 (1989).
- [50] V. Mizrahi, K.W. DeLong, G.I. Stegeman, M.A. Saifi, and M.J. Andrejco, *Opt. Lett.* **14**, 1140 (1989).
- [51] A.B. Aceves and J.V. Moloney, *Opt. Lett.* **17**, 1488 (1992).
- [52] E.N. Tsoy, C.M. de Sterke, and F.Kh. Abdullaev, *J. Opt. Soc. Am. B* **18**, 1144 (2001).
- [53] A. Peleg, Q.M. Nguyen, and Y. Chung, *Phys. Rev. A* **82**, 053830 (2010).
- [54] Y. Okawachi, O. Kuzucu, M.A. Foster, R. Salem, A.C. Turner-Foster, A. Biberman, N. Ophir, K. Bergman, M. Lipson, and A.L. Gaeta, *IEEE Photon. Technol. Lett.* **24**, 185 (2012).
- [55] M.A. Foster, A.C. Turner, M. Lipson, and A.L. Gaeta, *Opt. Express* **16**, 1300 (2008).
- [56] J.P. Gordon, *Opt. Lett.* **11**, 662 (1986).
- [57] Y. Kodama and A. Hasegawa, *IEEE J. Quantum Electron.* **23**, 510 (1987).
- [58] F.M. Mitschke and L.F. Mollenauer, *Opt. Lett.* **11**, 659 (1986).
- [59] D.J. Kaup and B.A. Malomed, *J. Opt. Soc. Am. B* **12**, 1656 (1995).
- [60] In fact, we also demonstrated this destabilization effect in section III A of Ref. [36].
- [61] The dimensionless distance z in Eq. (1) is $z = X/(2L_D)$, where X is the dimensional distance, $L_D = \tau_0^2/|\tilde{\beta}_2|$ is the dispersion length, τ_0 is the soliton temporal width, and $\tilde{\beta}_2$ is the second-order dispersion coefficient. The dimensionless time is $t = \tau/\tau_0$, where τ is time. $\psi = (\gamma_3\tau_0^2/|\tilde{\beta}_2|)^{1/2}E$, where E is the electric field and γ_3 is the cubic nonlinearity coefficient. The coefficient ϵ_q is related to the dimensional quintic nonlinearity coefficient γ_5 via $\epsilon_q = 2\gamma_5|\tilde{\beta}_2|/(\gamma_3^2\tau_0^2)$.
- [62] A similar propagation model without the quintic nonlinearity term was used in Ref. [36].
- [63] The coefficients g_0 and ϵ_3 in Eq. (7) are related to the dimensional linear gain and cubic loss coefficients ρ_1 and ρ_3 by $g_0 = 2\rho_1\tau_0^2/|\tilde{\beta}_2|$ and $\epsilon_3 = 2\rho_3/\gamma_3$. The coefficient ϵ_R is $\epsilon_R = 2\tau_R/\tau_0$, where τ_R is a dimensional time constant, characterizing the waveguide's delayed Raman response [4, 64]. The value of τ_R can be determined from the slope of the Raman gain curve of the waveguide [4, 64].
- [64] S. Chi and S. Wen, *Opt. Lett.* **14**, 1216 (1989).
- [65] Q.M. Nguyen and A. Peleg, *Opt. Commun.* **283**, 3500 (2010).
- [66] M. Nakazawa, E. Yamada, H. Kubota, and K. Suzuki, *Electron. Lett.* **27**, 1270 (1991).
- [67] M. Nakazawa, *IEEE J. Sel. Top. Quantum Electron.* **6**, 1332 (2000).

- [68] L.F. Mollenauer, A. Grant, X. Liu, X. Wei, C. Xie, and I. Kang, Opt. Lett. **28**, 2043 (2003).
- [69] Note that in Ref. [36], we used the same threshold values of 0.075 and 0.655 for determining the values of z_q and z_f from the simulations with the perturbed CNLS equation.
- [70] In addition to the growth of the radiative tail, the radiative tail near the soliton exhibits oscillatory (“breathing”) dynamics.
- [71] P.C. Becker, N.A. Olsson, and J.R. Simpson, *Erbium-Doped Fiber Amplifiers: Fundamentals and Technology* (Academic, San Diego, CA, 1999), chapter 8.
- [72] The duration of the simulation with $z_f = 200$ on a workstation equipped with a 3.90 GHz processor was about 36 hours. The long duration was mainly due to the large value of $\beta(z_f)$, $\beta(z_f) \simeq -230$, which made it necessary to employ a relatively large frequency domain $[-275, 275]$, and small time and distance steps $\Delta t = 0.014$ and $\Delta z = 0.00004$. For a simulation with $z_f = 400$, for example, the value of $\beta(z_f)$ predicted by Eq. (21) is $\beta(z_f) \simeq -476$. In this case, we would have to use a frequency domain $[-520, 520]$ or larger, and Δt and Δz values of $\Delta t = 0.007$ and $\Delta z = 0.00001$. As a result, the simulation duration on the same workstation would be 48 days or longer.
- [73] A. Hasegawa and Y. Kodama, *Solitons in Optical Communications* (Clarendon, Oxford, 1995).
- [74] E. Iannone, F. Matera, A. Mecozzi, and M. Settembre, *Nonlinear Optical Communication Networks* (Wiley, New York, 1998).
- [75] D.J. Kaup, Phys. Rev. A **42**, 5689 (1990).
- [76] A. Peleg and D. Chakraborty, Physica D **406**, 132397 (2020).
- [77] I.S. Gradshteyn and I.M. Ryzhik, *Table of Integrals, Series, and Products* (Academic, Amsterdam, 2007).
- [78] For both the CQNLs soliton and the CNLS soliton, the value of $y(z)$ is not changed by linear gain-loss or by cubic loss in first order in ϵ_3 . It is affected by the Raman perturbation in first order in ϵ_R only via the z dependence of the soliton’s frequency. However, second-order effects, which are beyond our perturbative calculation, might also induce appreciable changes in $y(z)$ at large distances. We therefore choose to measure $y(z)$ from the simulations, as was also done in Ref. [36].
- [79] M. Abramowitz and I.A. Stegun (Eds.), *Handbook of Mathematical Functions with Formulas, Graphs, and Mathematical Tables* (National Bureau of Standards, Washington, D.C., 1972).